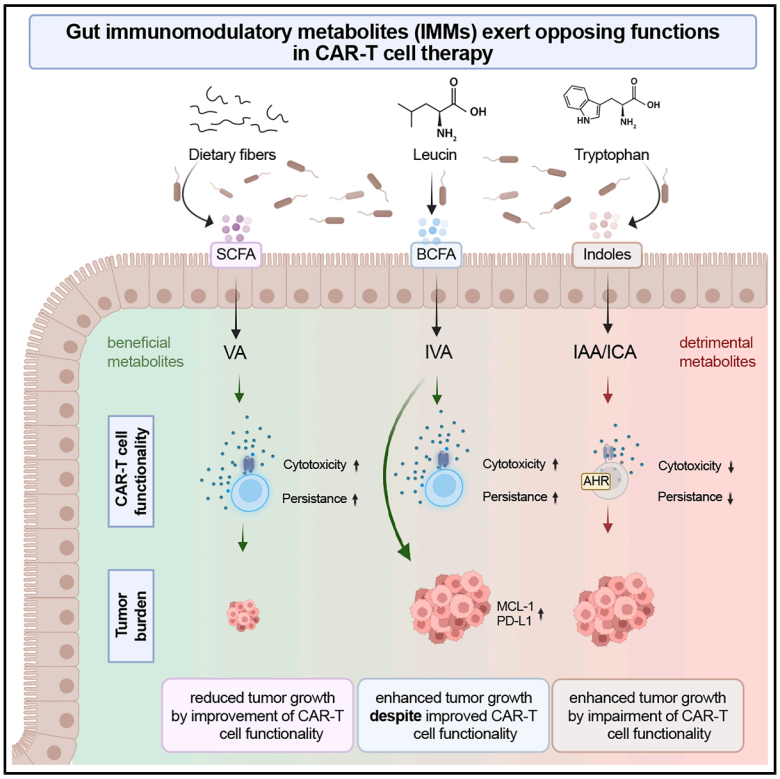
Cell

Opposing functions of gut immunomodulatory metabolites on CAR-T therapy

Graphical abstract



Highlights

- Pre-CAR-T gut microbiota poorly predicts clinical outcome across studies
- Gut metabolites exert opposing effects on CAR-T cell function and response
- Valeric acid enhances CAR-T fitness, metabolism, and antitumor activity
- Indoles impair CAR-T function, while isovaleric acid promotes tumor growth

Authors

Markus Perl, Severin Guetter, Dhyani Shah, Simon Holzinger, ..., Matthias A. Fante, Erik Thiele Orberg, Hendrik Poeck

Correspondence

markus.perl.ukr@gmail.com (M.P.), erik.orberg@ukr.de (E.T.O.), hendrik.poeck@ukr.de (H.P.)

In brief

Gut microbial taxonomy alone is a poor predictor of CAR-T cell therapy outcome. Instead, specific gut immunomodulatory metabolites exert opposing effects on CAR-T cell function and tumor control, identifying microbial metabolism as a potential target to predict and improve CAR-T cell outcomes.

Perl et al., 2026, Cell *189*, 6968–6987
October 29, 2026 © 2026 The Author(s). Published by Elsevier Inc.
https://doi.org/10.1016/j.cell.2026.09.004

CellPress

CellPress
OPEN ACCESS

Cell

Article

Opposing functions of gut immunomodulatory metabolites on CAR-T therapy

Markus Perl,[1,2,30,*] Severin Guetter,[1,3,30] Dhyani Shah,[1,3,30] Simon Holzinger,[1,3,30] Luisa Becker,[1] Misbah Tariq,[1] Philipp Menauer,[4] Simon Delahais,[4] Gloria Lutzny-Geier,[5] Julian N. Scherer,[1] Sascha Göttert,[1,3] Konstantin Herfeld,[1] Paul Heinrich,[3] Klaus Georg Kreitmeier,[1] Claudia Gebhard,[3] Wolfgang Herr,[1] Marcel P. Trefny,[4] Janina Doerr,[4] Saba Sameri,[1] Dennis C. Harrer,[1,3] Kai Ziegler-Martin,[6] Sarah Staudt,[6] Leo Hansmann,[1] Matthias Edinger,[1,3] Daniel Wolff,[1] Daniela Weber,[1] Elisabeth Meedt,[1] Alexander Denk,[1] Andre Gessner,[7] Ernst Holler,[1] Tobias Wertheimer,[8] Klaus Neuhaus,[9] Tingting Zheng,[10,11] David M. Cordas Dos Santos,[12] Sebastian Theurich,[13,14] Melanie Schirmer,[10,11,15] Karin Kleigrewe,[16] Jonas Schluter,[17,18] Marcel van den Brink,[19] Michael Schmitt,[20] Markus Feuerer,[3] Christoph Heuser-Loy,[3,21] Jeremy Baldwin,[3] Luca Gattinoni,[3] Michael Rehli,[1,3] Michael Hudecek,[6,22] Camille Bigenwald,[23] Laurence Zitvogel,[23] Marion Subklewe,[13,24,25,26] Viktoria Blumenberg,[13,24,25,26] Maria-Luisa Schubert,[20] Christoph Stein-Thoeringer,[27] Maik Luu,[6,22] Sebastian Kobold,[4,24,26,28] Matthias A. Fante,[1,29,30] Erik Thiele Orberg,[1,2,30,*] and Hendrik Poeck[1,2,3,30,31,*]

[1]Department of Internal Medicine III, Hematology & Internal Oncology, University Hospital Regensburg, Regensburg, Germany
[2]Bavarian Cancer Research Center (BZKF), Regensburg, Germany
[3]Leibniz Institute for Immunotherapy (LIT), Regensburg, Germany
[4]Division of Clinical Pharmacology, Department of Medicine IV, University Hospital, Ludwig Maximilian University (LMU) of Munich, Munich, Germany
[5]Department of Internal Medicine 5, Hematology and Oncology, University Hospital Erlangen, Friedrich-Alexander-Universität Erlangen-Nürnberg, Erlangen, Germany
[6]Lehrstuhl für Zelluläre Immuntherapie, Medizinische Klinik und Poliklinik II, Universitätsklinikum Würzburg, Würzburg, Germany
[7]Institute of Clinical Microbiology and Hygiene, University Hospital Regensburg, Regensburg, Germany
[8]Division of Hematology and Oncology, Department of Medicine, Freiburg University, Freising, Germany
[9]Core Facility Microbiome, ZIEL - Institute for Food & Health, Technische Universität München, Freising, Germany
[10]Translational Microbiome Data Integration, School of Life Sciences, Technical University of Munich, Freising, Germany
[11]ZIEL - Institute for Food & Health, Technische Universität München, Freising, Germany
[12]Gene Center and Department of Biochemistry, LMU Munich, Munich, Germany
[13]Department of Medicine III, Hematology/Oncology, LMU University Hospital and Gene Center, LMU Munich, Munich, Germany

(Affiliations continued on next page)

SUMMARY

Chimeric antigen receptor (CAR)-T cell therapy has transformed hematological cancer treatment, yet nearly half of patients still relapse or progress. Increasing evidence implicates the gut microbiome and antibiotic exposure as key modulators of clinical outcomes. In a cohort of 129 patients across three German centers, shotgun metagenomics and targeted mass spectrometry revealed that reduced short-chain fatty acids, particularly valeric acid, prior to CAR-T cell therapy correlated with increased risk of disease progression. Conversely, high levels of indole metabolites, including indole-3-carboxaldehyde and indole-3-acetic acid as well as the branched-chain fatty acid isovaleric acid, were linked to adverse outcomes. Functional validation in human and murine CAR-T cell models demonstrated that valeric acid supplementation enhanced, while indole-3-carboxaldehyde and isovaleric acid impaired, CAR-T cell efficacy. These findings reveal the opposing roles of immunomodulatory metabolites on CAR-T cell therapy, carrying significant implications for the design of metabolite-guided, microbiome-based therapeutics.

INTRODUCTION

Chimeric antigen receptor T cell therapy (CAR-T cell therapy) has marked an immunotherapeutic breakthrough in the treatment of hematologic malignancies, achieving high complete response (CR) rates of up to 80% in refractory patients. Yet only about 50% of patients maintain durable remissions, and many patients experience severe toxicities.[1–4] Identification and modulation of factors that causally affect therapeutic efficacy and side effects of CAR-T cell therapy are key to further improving patient outcomes. The gut microbiome profoundly modulates systemic immunity,[5,6] which, in turn, may impact CAR-T cell expansion,

 © 2026 The Author(s). Published by Elsevier Inc.
This is an open access article under the CC BY license (http://creativecommons.org/licenses/by/4.0/).

[14]German Cancer Consortium (DKTK), Partner Site Munich, a partnership between the DKFZ and BZKF at the University Hospital of the LMU, Germany
[15]Center for Organoid Systems, Technical University Munich, Garching, Germany
[16]Bavarian Center for Biomolecular Mass Spectrometry, TUM School of Life Sciences, Technical University Munich, Freising, Germany
[17]Department of Microbiology, New York University Grossman School of Medicine, New York, NY, USA
[18]Institute for Systems Genetics, NYU Langone Health Grossman School of Medicine, New York, NY, USA
[19]Beckman Research Institute, City of Hope, Duarte, CA, USA
[20]Department of Medicine V, Hematology, Oncology and Rheumatology, University Hospital Heidelberg, Heidelberg, Germany
[21]Department of Internal Medicine III, Haematology and Oncology, University Hospital Bonn, Bonn, Germany
[22]Branch Cellular Immunotherapy, Fraunhofer Institute for Cell Therapy and Immunology (IZI), Würzburg, Germany
[23]Gustave Roussy Cancer Campus, Villejuif, France
[24]Laboratory for Translational Cancer Immunology, Gene Center LMU Munich, Munich, Germany
[25]German Cancer Consortium (DKTK), Partner Site Munich, Munich, Germany
[26]Bavarian Cancer Research Center (BZKF), Munich, Germany
[27]Department of Internal Medicine I, University Hospital Tuebingen, Tuebingen, Germany
[28]German Center for Lung Research (DZL), Partner Site Munich, Munich, Germany
[29]Department of Internal Medicine II, University Hospital of Würzburg, Würzburg, Germany
[30]These authors contributed equally
[31]Lead contact
*Correspondence: markus.perl.ukr@gmail.com (M.P.), erik.orberg@ukr.de (E.T.O.), hendrik.poeck@ukr.de (H.P.)
https://doi.org/10.1016/j.cell.2026.09.004

persistence, and toxicity. Thereby, detrimental perturbation of the intestinal microbiome in a process termed intestinal dysbiosis (ID) is characterized by a loss of symbiotic commensals and overgrowth of pathobionts. This is commonly caused by broad-spectrum antibiotics that are used in more than 20% of patients receiving CAR-T cell therapy. ID impairs immunotherapies, including immune-checkpoint inhibitors (ICIs), allogeneic stem cell transplantation (allo-SCT), and CAR-T cell therapy.[7–11]

Recent studies indicate that immunomodulatory metabolites (IMMs) derived from the gut directly influence immunotherapy outcomes.[12] Among these metabolites, short-chain fatty acids (SCFA), trimethylamine N-oxide (TMAO), and inosine produced by commensal anaerobes in the gut have been linked to improved CAR-T cell outcomes.[11,13–15]

Although many studies have explored the role of beneficial commensal metabolites in immunotherapy—with increasing literature on CAR-T cell outcomes—bacterial metabolites may have diverse immunomodulatory effects, and none have investigated the detrimental effects of microbial metabolites as a feature of ID.[16]

Here, we conducted a comprehensive analysis of gut microbiota using shotgun metagenomics alongside gut and serum metabolite profiling in recipients of CAR-T cell therapy, demonstrating that IMMs exert opposing effects on CAR-T cell therapy and serve as superior predictors of outcomes compared with individual bacterial taxa. These findings have important implications for developing microbiota-based strategies to enhance CAR-T cell therapy.

RESULTS

Patient collective and outcomes

Between 2020 and 2024, 129 patients receiving CAR-T cell therapy were enrolled across three large German centers (Table 1; Figure 1A) to identify microbial signatures predictive of treatment outcomes, with a mean follow-up of 360 days (22 to 1,492 days). Main indications were diffuse large B cell lymphoma (DLBCL; n = 80, 62%) and multiple myeloma (MM; n = 24, 18.6%) and mantle cell lymphoma (n = 11, 8.5%). CR at day 180 (as defined by the Lugano criteria for non-Hodgkin lymphoma [NHL], International Myeloma Working Group [IMWG] criteria for MM, and response evaluation criteria in solid tumors [RECIST] for solid tumors) was achieved by n = 51 (39.5%), partial response (PR) by 19 (14.7%), stable disease (SD) by 5 (3.9%), and progressive disease (PD) by 53 (41.1%) patients. Most patients experienced cytokine release syndrome (CRS; n = 119, 92.2%) that was ≥grade 2 in n = 71 (55.4%) patients; some experienced immune effector cell associated neurotoxicity syndrome (ICANS; n = 39, 30.2%) that was ≥grade 2 in 29 cases (22.6%). Antibiotics were used in n = 35 (27.1%) patients within 28 days prior to CAR-T cell infusion, with most patients receiving piperacillin/tazobactam (n = 22, 17.1%) and meropenem (n = 14, 10.9%). Here, we perform unbiased multi-omics profiling of patient samples collected at hospital admission for CAR-T cell therapy (median sampling day was day –4 relative to CAR-T cell therapy, sampling time points included in Table 1) to identify microbial signatures that correlate with clinical responses (Figure 1A): fecal metabolomics was performed in 111 (86%), serum metabolomics in 98 (76%), and metagenomics in 56 (43.3%) patients.

Antibiotic therapy prior to CAR-T cell infusion is associated with adverse outcomes, decreased microbial diversity, and microbial metabolic output

Previous studies indicate that antibiotic exposure within the first month prior to lymphodepletion affects anti-CD19 CAR-T cell therapy outcomes.[8–11,14,17] Similarly, in our cohort, patients exposed to any antibiotics (excluding cotrimoxazole and azithromycin pneumocystis prophylaxis) up to 28 days before CAR-T cell infusion had worse progression-free survival (PFS; hazard ratio [HR] 1.8, p = 0.013) and overall survival (OS; HR 4.4, $p < 0.001$; Figure S1A) than patients not exposed to antibiotics. Patients treated with antibiotics before CAR-T cell therapy had lower microbial richness and trended to lower diversity and increased dominance, as measured by observed richness, the Shannon

Table 1. Patient characteristics

	Overall	Regensburg	Heidelberg	Munich
Total	129 (100)	73 (56.6)	36 (27.9)	20 (15.5)
Age mean – year (min-max)	61.5 (29–82)	62.1 (29–77)	60.2 (31–82)	61.8 (30–73)
Male sex (%)	73 (56.6)	37 (50.7)	28 (77.8)	8 (40)
ECOG				
0	40 (31)	16 (21.9)	19 (52.8)	5 (25)
1	73 (56.6)	44 (60.3)	17 (47.2)	12 (60)
2	13 (10.1)	12 (16.4)	0 (0)	1 (5)
3	2 (1.6)	1 (1.4)	0 (0)	1 (5)
NA	1 (0.8)	0 (0)	0 (0)	1 (5)
LDH at admission mean (min-max)	289.4 (113–1,421)	259.7 (114–1,273)	352 (168–1,421)	284.9 (161–522)
CAR-T cell product				
Axicabtagene ciloleucel	59 (45.7)	23 (31.5)	22 (61.1)	14 (70)
Tisagenlecleucel	17 (13.2)	10 (13.7)	5 (13.9)	2 (10)
Brexucabtagen autoleucel	16 (12.4)	8 (11.0)	6 (16.7)	2 (10)
Idecabtagen vicleucel	13 (10.1)	13 (17.8)	0 (0)	0 (0)
Ciltacabtagen autoleucel	11 (8.5)	10 (13.7)	0 (0)	1 (5)
Lisocabtagen maraleucel	6 (4.7)	2 (2.7)	3 (8.3)	1 (5)
Others	7 (5.4)	7 (9.6)	0 (0)	0 (0)
Time from treatment to sampling mean – days (SD)	−4.21 (7.66)	−4.26 (5.62)	−10.17 (12.72)	1.35 (2.78)
Follow-up mean (min-max)	360 (22–1,492)	386 (22–1,492)	312 (26–1,414)	352.5 (25–729)
Disease				
DLBCL	80 (62)	34 (46.6)	30 (83.3)	16 (80)
MM	24 (18.6)	23 (31.5)	0 (0)	1 (5)
MCL	11 (8.5)	5 (6.9)	5 (13.9)	1 (5)
ALL	4 (3.1)	3 (4.1)	0 (0)	1 (5)
FL	4 (3.1)	3 (4.1)	0 (0)	1 (5)
Solid tumor	5 (3.9)	5 (6.9)	0 (0)	0 (0)
Response at day 180				
PD	53 (41.1)	33 (45.2)	14 (38.9)	6 (30)
CR	51 (39.5)	29 (39.7)	13 (36.1)	9 (45)
PR	19 (14.7)	8 (11.0)	7 (19.4)	4 (20)
SD	5 (3.9)	3 (4.1)	1 (2.8)	1 (5)
not reached	1 (0.8)	0 (0)	1 (2.8)	0 (0)
CRS (any grade)	119 (92.2)	65 (89.0)	32 (88.9)	17 (85)
Grade 1	43 (33.3)	20 (27.4)	13 (36.1)	10 (50)
Grade 2	58 (45.0)	35 (48.0)	19 (52.8)	4 (20)
Grade 3	11 (8.5)	9 (12.3)	0 (0)	2 (10)
Grade 4	2 (1.6)	1 (1.4)	0 (0)	1 (5)
ICANS (any grade)	39 (30.2)	17 (23.3)	15 (41.7)	7 (35)
Grade 1	10 (7.8)	5 (6.9)	4 (11.1)	1 (5)
Grade 2	15 (11.6)	5 (6.9)	9 (25)	1 (5)
Grade 3	6 (4.65)	3 (4.1)	1 (2.8)	2 (10)
Grade 4	8 (6.2)	4 (5.5)	1 (2.8)	3 (15)
Antibiotics used prior to CAR-T cell therapy	35 (27.1)	18 (24.7)	8 (22.2)	9 (45)
Any broad spectrum with anaerobe coverage (PIM)	27 (20.9)	10 (13.7)	8 (22.2)	9 (45)

(*Continued on next page*)

Table 1. *Continued*

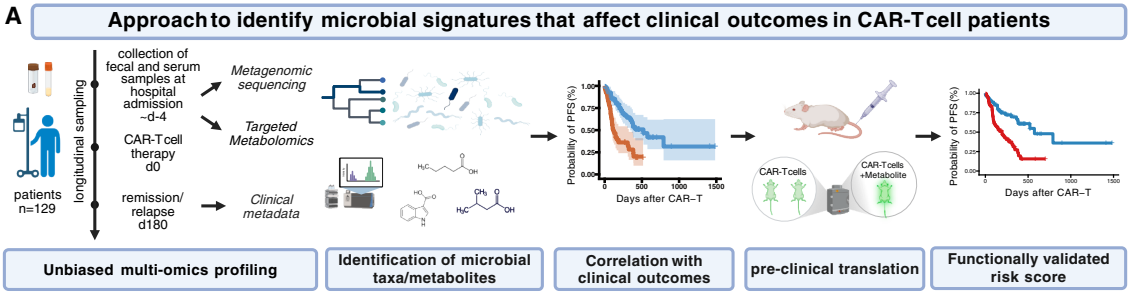
	Overall	Regensburg	Heidelberg	Munich
Piperacillin/tazobactam	22 (17.1)	8 (11.0)	5 (13.9)	9 (45)
Meropenem	14 (10.9)	7 (9.6)	2 (5.6)	5 (25)
Vancomycin (i.v.)	10 (7.8)	6 (8.2)	2 (5.6)	2 (10)
Amoxicillin/clavulanic acid	3 (2.3)	2 (2.7)	0 (0)	1 (5)
Ciprofloxacin	3 (2.3)	3 (4.1)	0 (0)	0 (0)
Ceftazidim	2 (1.6)	1 (1.4)	0 (0)	1 (5)
Linezolid	1 (0.8)	1 (1.4)	0 (0)	0 (0)
Moxifloxacin	1 (0.8)	1 (1.4)	0 (0)	0 (0)
Flucloxacillin	1 (0.8)	0 (0)	0 (0)	0 (0)
Azithromycin	2 (1.6)	0 (0)	1 (2.8)	1 (5)
Pivmecillinam	1 (0.8)	1 (1.4)	0 (0)	0 (0)
Fecal metabolomics available	111 (86)	68 (93.2)	33 (91.7)	10 (50)
Serum metabolomics available	98 (76)	67 (91.8)	17 (47.2)	14 (70)
Metagenomics available	56 (43.4)	56 (76.7)	0 (0)	0 (0)

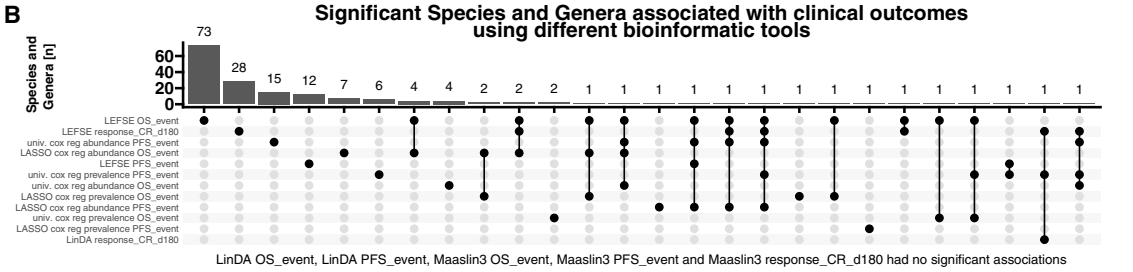
index and the Berger-Parker index, respectively (Figure S1B). However, reduced diversity and richness as well as increased microbial dominance only showed a trend toward poorer PFS and OS (Figures S1C and S1E). Antibiotics were linked to lower levels of fecal microbial metabolites, including SCFAs (Figure S2A) and branched-chain fatty acids (BCFAs) (Figure S2B). By contrast, indole derivatives were only slightly lower in antibiotics-pretreated individuals compared with those who were not treated with antibiotics (Figure S2C). Secondary bile acids deoxycholic and lithocholic acid were lower in antibiotics-treated patients, while most other fecal bile acids did not show significant differences (Figure S2D). Thus, we confirmed the negative impact of antibiotics administered prior to CAR-T cell therapy on therapeutic outcomes, as well as their harmful effects on microbial diversity, fecal SCFAs, and BCFAs (Figures S1A, S1B, S2A, and S2B). Interestingly, fecal indole derivative indole-3-acetic acid (IAA) and various primary and secondary bile acids were not deregulated after antibiotic treatment (Figures S2C and S2D).

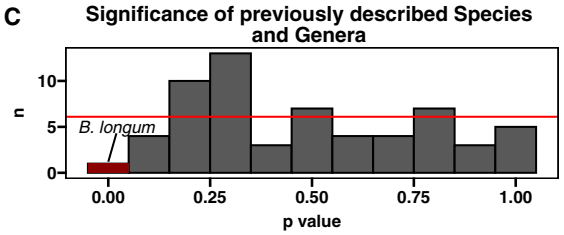
Commensal anaerobes, but not single bacterial strains, correlate with improved PFS after CAR-T cell therapy and microbial metabolites

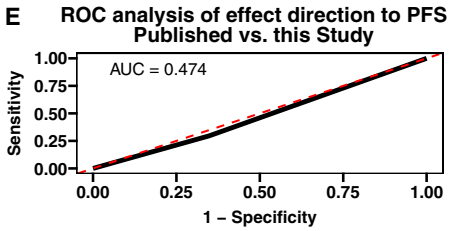
Given that we could validate the association of antibiotics with both outcome and fecal microbial diversity measures, we evaluated fecal microbial taxa and pathways derived from metagenomic sequencing with feces sampled at hospital admission for CAR-T. Metagenomic sequencing identified $n = 1{,}188$ distinct microbial species in the feces, with many of these only found in single individuals ($n = 401$). Various bioinformatic approaches identified significant associations between microbes and CAR-T cell outcomes but showed minimal overlap in species significantly associated with CR at day 180, PFS, or OS, both across outcomes and between methods (Figure 1B). Furthermore, we analyzed species and genera that were previously linked to improved CAR-T cell outcomes in other studies (Table S1[8–10,13,18]). Of these species and genera, only the *Bifidobacterium longum* species was significantly associated with improved PFS in our cohort using univariate Cox regression (Figure 1C). Patients with detectable levels of *B. longum* had longer PFS (HR = 0.48, $p = 0.034$; Figure 1D) and OS (HR = 0.15, $p = 0.016$; Figure S3A) compared with patients with non-detectable levels. *B. longum* was associated with the SCFA valeric acid in the stool of patients but not with the BCFA isovaleric acid or indole derivatives IAA and indole-3-carboxaldehyde (ICA) (Figure S3B). In our cohort, the effect direction (toward longer PFS/better response rates or shorter PFS/lower response rates) of previously published species and genera (such as *Ruminococcus gnavus* and *Akkermansia muciniphila*[8,18]; Figures S3C and S3D) did not replicate the published effect on PFS, with an area under the curve (AUC) in a receiver operating characteristic (ROC)-like analysis of 0.474 (Figure 1E), indicating matching directions no better than random chance. Microbial profiles of patients did not cluster according to CR at day 180 after CAR-T in a non-metric multidimensional scaling (NMSD) analysis based on Bray-Curtis dissimilarities (PERMANOVA, $R^2 = 0.023$, $p = 0.141$; Figure S3E). This may be attributed to the highly heterogeneous fecal microbial taxa of patients on a species level with a mean Bray-Curtis dissimilarity index of 0.87 between patients (Figure 1F). Given that microbial species and genera did not robustly predict patient survival, we investigated whether specific microbial pathways were associated with CAR-T cell outcomes. Pathways related to anaerobic energy metabolism (i.e., PWY-7389 and PWY-7384) or fatty acid synthesis (i.e., PWY-5994) were (in trend) linked to improved PFS in univariate Cox regression, while pathways involving aerobic metabolism (i.e., PWY-7279 and PWY-3781) were associated with poor PFS (Figure 1G). Additionally, principal-component analysis revealed distinct grouping of microbial metabolites but not microbial species (Figure S3F). The clustering of microbial metabolites also seemed predictive for CRs at day 180 after CAR-T infusion.

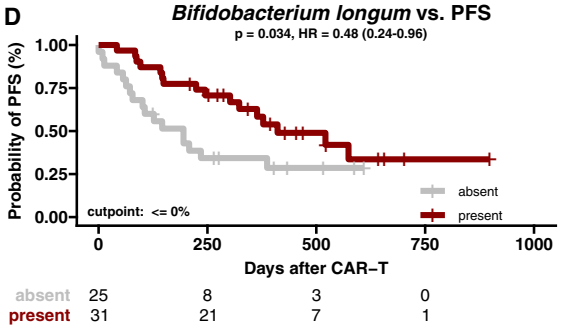
Thus, microbial taxonomic composition appeared to be a weak predictor of therapeutic outcomes, whereas microbial metabolism—specifically, the opposing roles of aerobic and anaerobic pathways—showed stronger associations, with aerobic metabolism linked to poorer outcomes and anaerobic metabolism at least in trend associated with better outcomes.

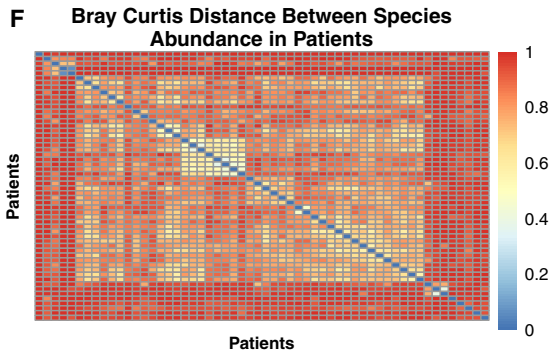


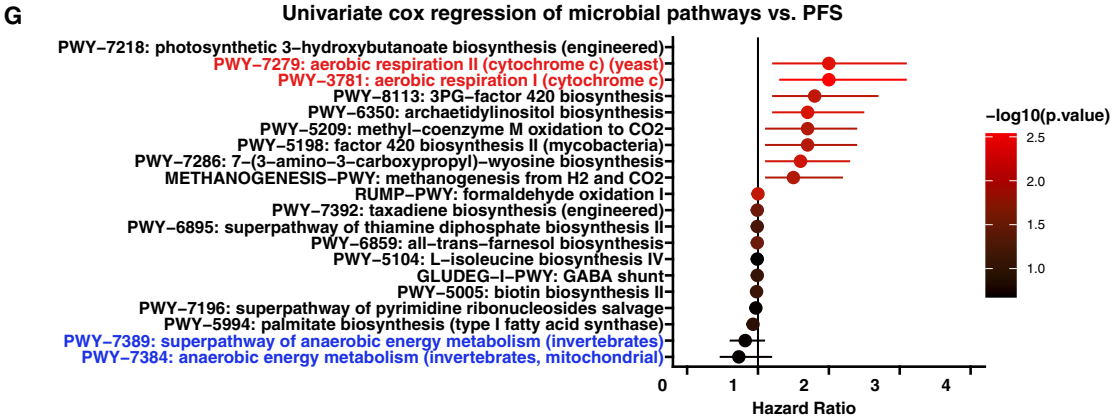












(legend on next page)

IMM profiles are predictive for CAR-T cell outcomes

Since microbial metabolism pathways were linked to CAR-T cell outcomes, we tested whether metabolic output better predicts CAR-T cell outcomes than microbial diversity, single species, or genera. Unsupervised hierarchical clustering of fecal IMM profiles identified a subgroup of 34 patients with low concentrations of IMMs (Figure 2A). This group experienced reduced PFS ($p < 0.0001$, HR = 2.84) and OS ($p < 0.0001$, HR = 6.48; Figure 2B) compared with all other patients. Interestingly, not all IMM-proficient patients responded similarly; one group had higher IMM levels in only two of the four metabolite clusters and appeared to have intermediate survival rates compared with the other two groups (Figure 2A).

Fecal IMMs are associated with beneficial and detrimental outcomes

These observations led to further investigation of the association of individual IMMs with CAR-T cell outcomes. High fecal (i.e., above cutoff based on maximum log-rank statistics) levels of specific SCFAs (acetic acid, butyric acid, and valeric acid) correlated with improved PFS and OS (Figures 2C and S4A). High levels of BCFAs isobutyric, 2-methylbutyric, and isovaleric acid (Figures 2D and S4B) and indole derivatives IAA and ICA were linked to worse PFS (Figures 2E and S4C) but not OS except for IAA, suggesting a potential ambivalent role for microbial metabolites in CAR-T cell therapy. Of note, indole-3-propionic acid (IPA), an indole conjugated with the SCFA propionic acid trended to positive associations with both PFS and OS (Figure S4C). Taken together, metabolite profiles as well as single metabolites were predictive for CAR-T cell outcomes, SCFAs (especially valeric acid) were associated with improved, indoles and BCFAs with poor outcomes.

Serum IMMs resemble fecal associations to beneficial and detrimental outcomes

Next, we explored the association of serum IMMs to CAR-T cell outcomes since previous publications have partially relied on serum metabolomic data.[18] Hierarchical clustering of serum metabolites (Figure 3A) revealed a cluster of patients that had higher levels of BCFAs with poor response rates and a significantly shorter PFS ($p < 0.0001$, HR = 4.39) and OS ($p < 0.0001$, HR = 5.67) compared with all other clusters (Figure 3B). In accordance with fecal levels, serum levels of single IMMs such as the SCFAs butyric and valeric acid were predictive for longer and isovaleric acid for shorter PFS (Figures 3C and 3D), while the indole IAA (Figure 3E) was (in trend) associated with worse PFS. Of note, ICA showed very low serum levels and no correlation to either PFS or OS.

IMMs directly shape CAR-T cell function *in vitro*

To assess whether the observed clinical associations of metabolites to CAR-T cell outcomes were causal, we examined the effects of metabolites on CAR-T cells *in vitro*. As we found correlations of the key IMM classes SCFAs, BCFAs, and indoles both to beneficial and detrimental outcomes, we chose valeric acid, isovaleric acid, ICA, and IAA as representative metabolites for further analysis to experimentally validate these opposing associations. As clinically relevant model systems of CAR-T cells directed at hematological and solid-cancer targets, we used human anti-CD19 and anti-HER2 CAR-T cells to confirm applicability across different CAR-T cell targets. Human anti-HER2 CAR-T cells were activated on HER2 protein-coated plates in the presence of these metabolites for 72 h. Flow cytometry analysis revealed that treatment with 1,000 μM valeric and isovaleric acid increased the expression of cytotoxic transcription factors and effector molecules, including T-bet, Eomes, interferon (IFN)-γ, and granzyme B in both $CD4^+$ and $CD8^+$ subsets relative to carrier-treated controls. By contrast, ICA and IAA were titrated at two concentrations and suppressed these functional markers in a dose-dependent manner, with the higher concentration exerting the stronger effect (Figure 4A). Consistently, ICA or IAA impaired CAR-T cell proliferation, whereas valeric and isovaleric acid did not (Figure S5A). The suppressive effects of IAA and ICA, as well as the immunostimulatory effects of valeric and isovaleric acid, were also replicated with anti-CD19 CAR-T cells. Like anti-HER2 CAR-T cells, valeric and isovaleric acid increased, while ICA and IAA decreased the expression of cytotoxic transcription factors and markers (Figure S5B).

Guided by these results, cytotoxicity assays used a single predefined dose of 1,000 μM for valeric/isovaleric acid and, for ICA/IAA, only the higher, more effective dose of 500 μM. A 72-h pretreatment with valeric or isovaleric acid enhanced target cell killing of $HER2^+$ SKOV3 and $CD19^+$ NALM-6 cells by anti-HER2 and anti-CD19 CAR-T cells, respectively, whereas pretreatment with ICA or IAA significantly reduced target cell killing (Figure 4B).

Figure 1. Microbial pathways and metabolites, but not single microbial species, are predictive for CAR-T cell outcomes

(A) Study design.

(B) Upset plot visualizing the overlap of microbial species and genera associated with clinical outcomes (CR d180, OS, and PFS) identified with different bioinformatic methods.

(C) Histogram of *p* values from univariate Cox regression analyses of previously published predictive species and genera vs. PFS in this study.

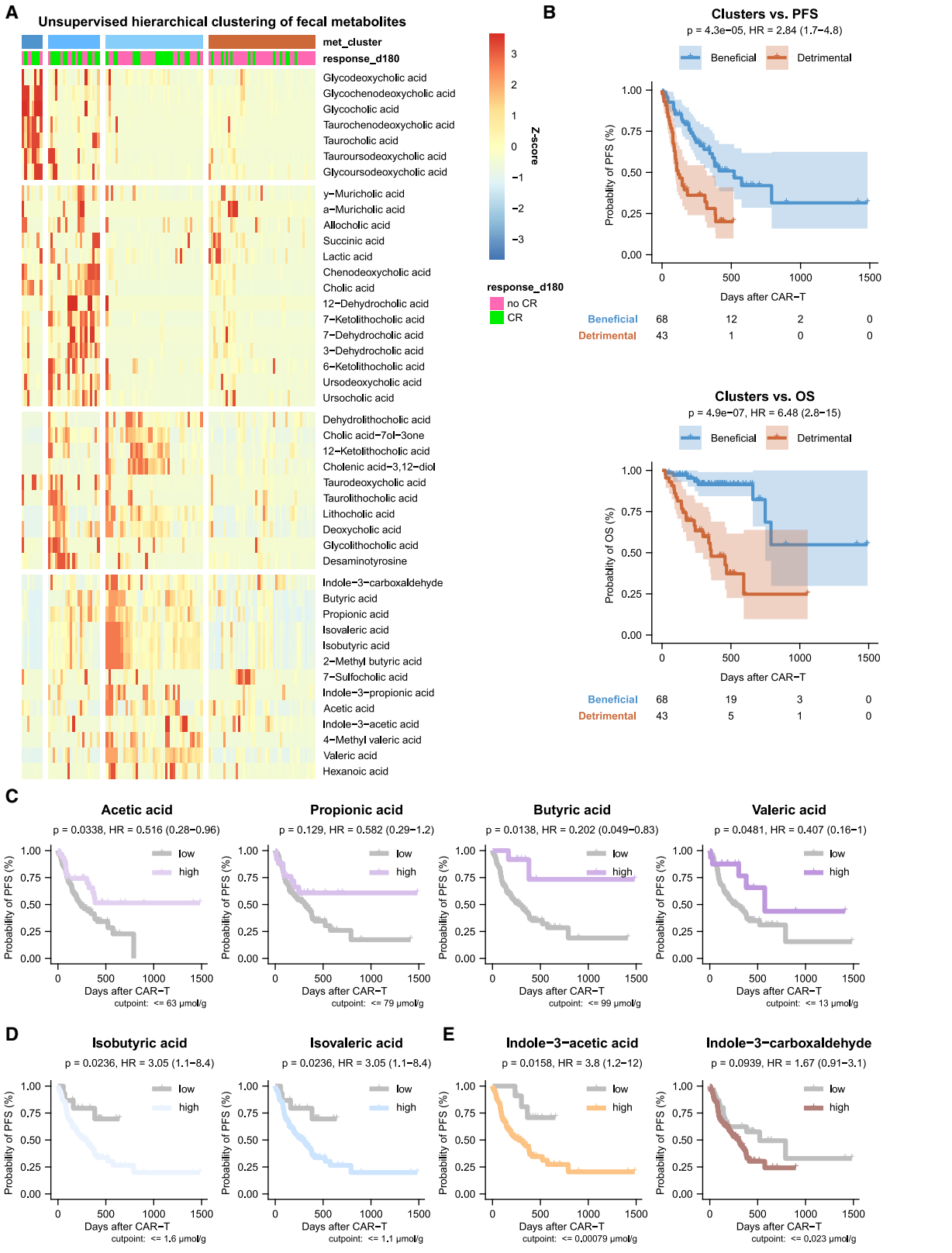
(D) PFS of patients stratified by presence or absence of *Bifidobacterium longum*. Patients with detectable *Bifidobacterium longum* show longer PFS (two-sided log-rank test, $p = 0.034$, HR = 0.48).

(E) ROC-like analysis comparing published species and genera effect directions with those observed in this cohort reveals no predictive value of previous descriptions.

(F) Bray-Curtis dissimilarity analysis for all microbial species and patients analyzed in this study shows a highly dissimilar microbiome on a species level within the cohort (mean Bray-Curtis distance 0.87).

(G) Forest plot of univariate Cox regression of microbial pathways vs. PFS reveals aerobic energy metabolism among the pathways with the strongest association with adverse PFS (annotated in red) and anaerobic metabolism (annotated in blue) with improved PFS. The ten pathways with the lowest *p* value for positive and negative associations, respectively, are depicted. Error bars indicate a 95% confidence interval (CI).

See also Figures S1–S3.



(legend on next page)

To uncover the underlying molecular mechanisms, we chose one IMM from the group of SCFAs (valeric acid), BCFAs (isovaleric acid), and indoles (ICA) and performed single-cell RNA sequencing (scRNA-seq) of HER2 protein-stimulated anti-HER2 CAR-T cells in the presence of IMMs *in vitro*. Graph-based clustering with Azimuth and marker gene expression-based annotation (Figure S6) showed profound differences between the treatments. ICA treatment led to the emergence of a cluster constituting terminally exhausted, dysfunctional CD3D$^-$, *TCF7*$^-$, *FOXP1*$^+$, and *TOX*$^+$ *CD4* T cells (CD4 terminally exhausted, log2FC = 3.15, $p < 0.0001$) and downregulation of *GZMB*$^+$ and *GNLY*$^+$ CD4$^+$ cytotoxic clusters (CD4 cytotoxic [*IFNG*-], log2-fold change = −1.48, $p < 0.0001$ and CD4 cytotoxic [*IFNG*+], log2-fold change = −0.47, $p = 0.006$). By contrast, these CD4$^+$ cytotoxic clusters were upregulated with either isovaleric (CD4 cytotoxic [*IFNG*-], log2-fold change = 3.27, $p < 0.0001$ and CD4 cytotoxic [*IFNG*+], log2-fold change = 1.77, $p < 0.0001$) or valeric acid (CD4 cytotoxic [*IFNG*-], log2-fold change = 3.24, $p < 0.0001$ and CD4 cytotoxic [*IFNG*+], log2-fold change = 2.13, $p < 0.0001$) treatment compared with carrier-treated cells (Figures 4C and S6). Next, we examined differentially regulated pathways in CD4$^+$ and CD8$^+$ CAR-T cells using gene set enrichment analysis (Figure 4D). In the presence of ICA, we observed upregulation of the aryl hydrocarbon receptor (AHR) pathway, the cellular sensor for indoles.[19,20] Furthermore, negative regulation of cell cycle, a suppressive pathway, was upregulated, while activating pathways (T cell-mediated cytotoxicity and IFN-γ signaling) were downregulated. By contrast, treatment with isovaleric or valeric acid upregulated T cell activating pathways (including T cell activation and TNFA signaling via NFKB and IFN-γ signaling). Reactome database-annotated translation (only for isovaleric acid) and metabolism of amino acid and derivatives pathways were increased, while glucose metabolism (only for valeric acid in CD8$^+$ cells) was reduced. Accordingly, CRISPR-Cas9-mediated deletion of the *AHR* gene reversed the detrimental effects of ICA, including reduced killing of NALM-6 cells by anti-CD19 CAR-T cells *in vitro* (Figure S7A) and restored the expression of T cell effector markers during artificial stimulation of anti-HER2 CAR-T cells (Figure S7B).

Valeric and isovaleric acid seemed to influence metabolic pathways of CAR-T cells in scRNA-seq similar to our previous results, including shifts in glucose, amino acid and fatty acid metabolism.[14] When assessing these CAR-T cell metabolic features with SCENITH (single-cell energetic metabolism by profiling translation inhibition), valeric and isovaleric acid increased overall protein translation, a feature of total metabolic fitness,[21] unlike ICA and IAA that did not (Figure S8A). Valeric and isovaleric acid induced a metabolic shift toward lower glucose dependence and higher fatty acid and amino acid oxidation capacity (Figure S8B). Mechanistically, isovaleric acid increased phosphorylation of pyruvate dehydrogenase (PDH), a limiting factor of glucose-derived pyruvate into the citric acid cycle, and acetyl-coenzyme A (CoA) carboxylase (ACC; Figure S8C), which facilitates fatty acid uptake to mitochondria and fatty acid oxidation. Furthermore, valeric and isovaleric acid-treated CAR-T cells showed an increase in phosphorylated mechanistic target of rapamycin (mTOR) and phosphorylated S6 (Figure S8C), indicating engagement of the activating mTOR-S6 axis. Thereby, valeric and isovaleric acid-treated cells are metabolically more active and enter a multifuel, less glucose-dependent program. We also observed a strong increase in histone H3K9 acetylation (H3K9ac; Figure S8D) in CAR-T cells, with ∼8-fold elevation after valeric and isovaleric acid treatment, which could be further corroborated by an HDAC2 inhibition assay demonstrating direct activity of valeric and isovaleric acid on HDAC2 (Figure S8E).

Taken together, the identified IMMs showed immunomodulatory effects on CAR-T cells independent of the CAR-T cell target antigen. Valeric acid thereby increased engagement of the mTOR-S6 axis, directly inhibited HDAC2, and enhanced CAR-T cell cytotoxicity, consistent with its association to improved outcomes. ICA decreased CAR-T cell cytotoxicity in an AHR pathway dependent way in line with its association with adverse outcomes. However, isovaleric acid enhanced CAR-T cell killing and functioned similarly to valeric acid, unlike their opposing associations to PFS in patients.

Oral valeric acid supplementation improves, while ICA and isovaleric acid supplementation impair, CAR-T cell efficacy *in vivo*

We previously demonstrated a beneficial role of valeric acid pretreatment on adoptively transferred CAR-T cells.[13,14] Here, we questioned if oral metabolite supplementation would affect CAR-T cell efficacy in an immunocompetent model of murine CD19$^+$ A20 lymphoma. Mice were gavaged with carrier, ICA, valeric, or isovaleric acid and treated with syngeneic anti-CD19 CAR-T cells (Figure 5A; Data S1 for *in vivo* imaging system [IVIS] scans).

Gavage with ICA led to higher tumor burden and earlier disease progression, reduced CAR-T cell expansion, and reduced survival in comparison to vehicle-treated mice (Figures 5B–5D). By contrast, supplementation with valeric acid reduced disease progression, enhanced CAR-T cell expansion, and prolonged survival of CAR-T cell-treated mice compared with carrier-treated mice (Figures 5B–5D). Supplementation with isovaleric

Figure 2. The fecal IMM profile and single IMMs predict survival

(A) Unsupervised hierarchical clustering of winsorized and z-scaled stool metabolite levels reveals a cluster of patients that lack IMMs and shows low CR rates at d180 (brown annotation); metabolite-proficient patients have higher CR rates with considerable heterogeneity among clusters.

(B) The metabolite-deficient cluster shows shorter PFS and OS compared with metabolite-proficient clusters.

(C) High levels of SCFA acetic, propionic, butyric, and valeric acids are associated with improved PFS.

(D and E) High levels of BCFAs (D; isobutyric and isovaleric acid) and indoles (E; IAA and ICA) are associated with shorter PFS. Cutoffs in (C)–(E) were determined using maximally selected rank statistics and are annotated below. Of note: isobutyric and isovaleric acids are highly correlated; different cutpoints result in the same grouping of patients. All *p* values reported correspond to two-sided log-rank tests, and hazard ratios were estimated from Cox proportional hazards models.

See also Figure S4.

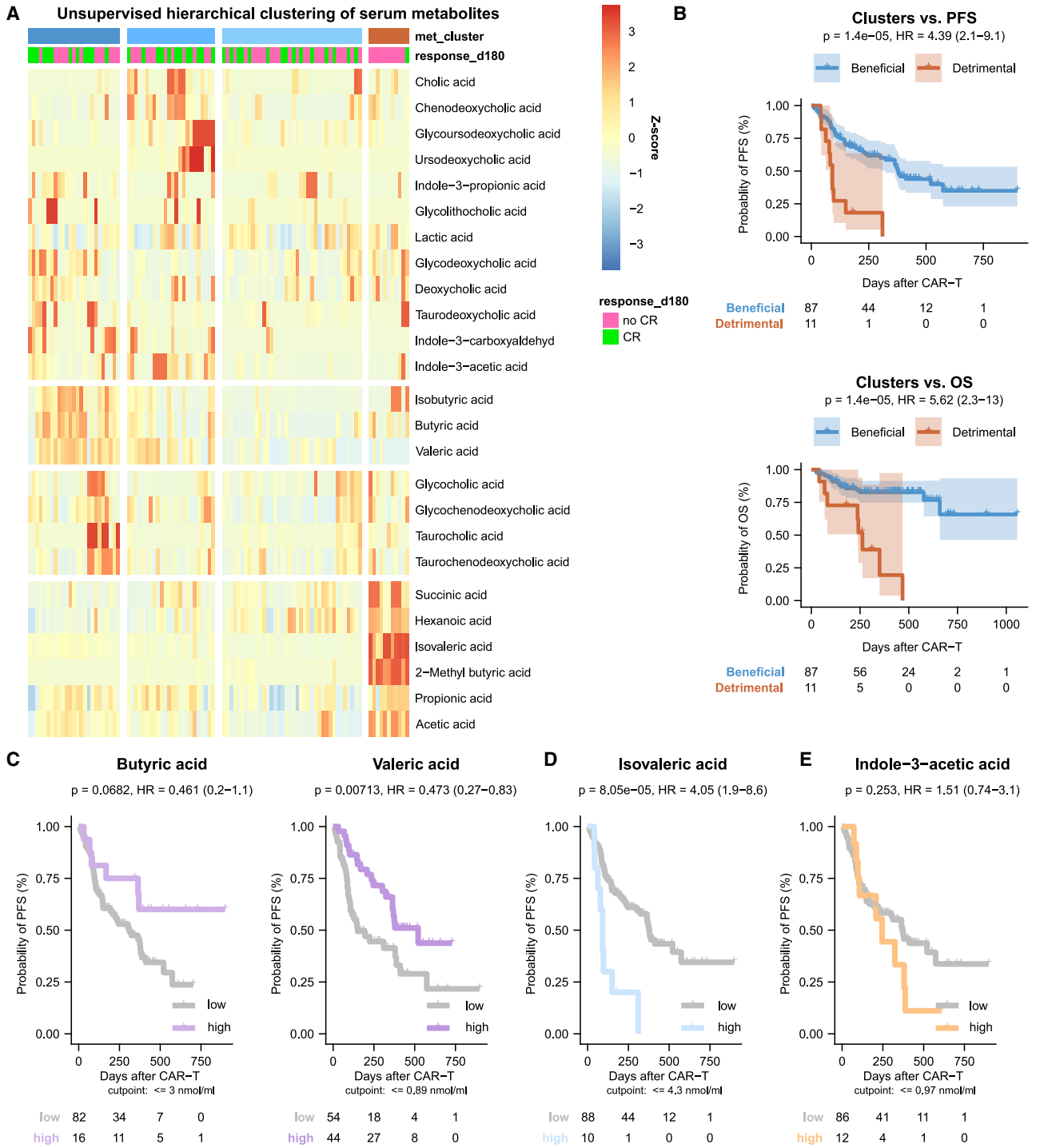


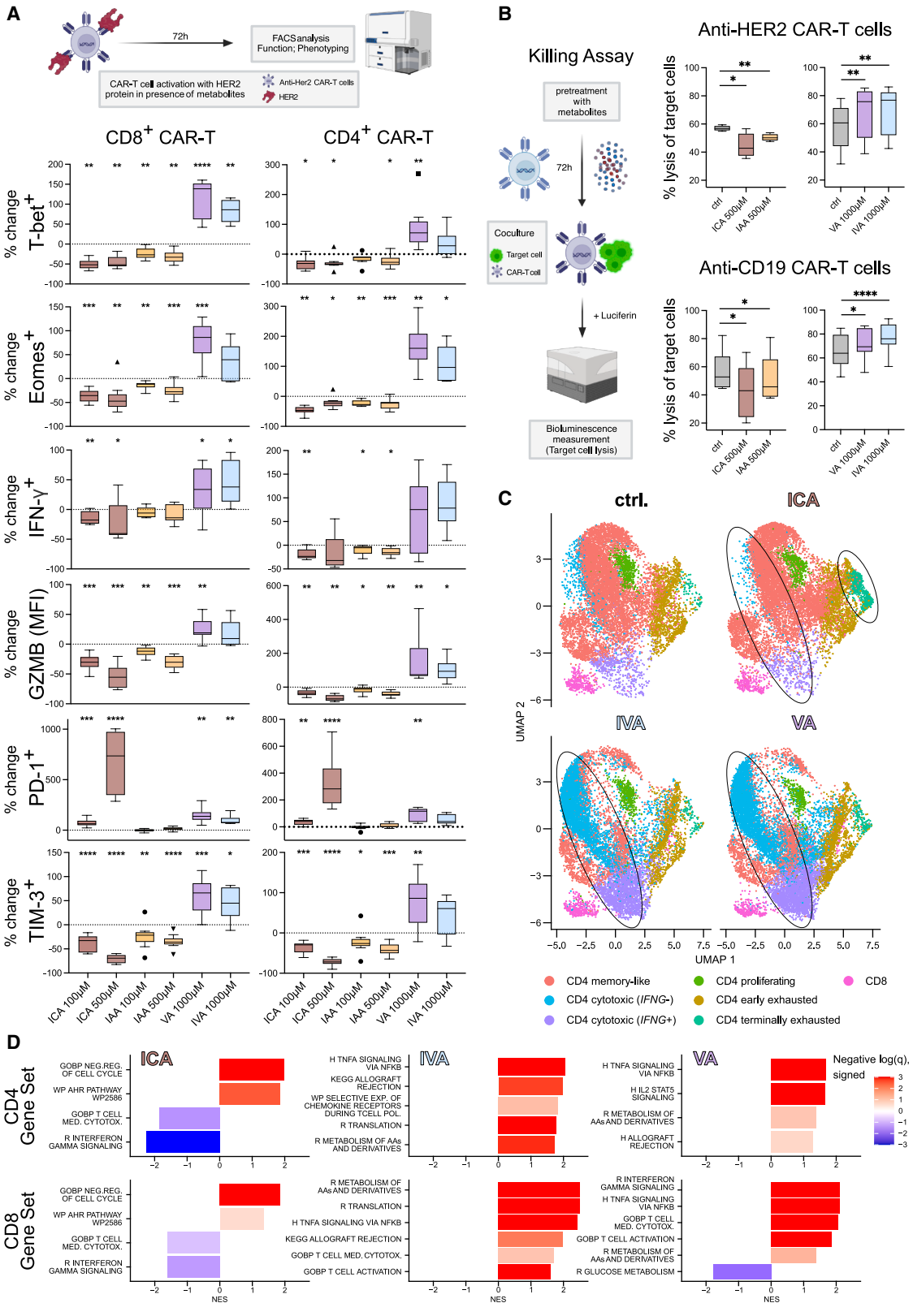
Figure 3. The serum IMM profile and single IMMs predict survival

(A) Unsupervised hierarchical clustering of winsorized and z-scaled serum metabolite levels reveals a cluster of patients that show low CR rates at d180 (brown annotation) and upregulate BCFAs; the other clusters have higher CR rates with considerable heterogeneity among clusters.

(B) These beneficial clusters show longer PFS and OS compared with the detrimental cluster.

(C) High levels of SCFAs butyric and valeric acids are associated with improved PFS.

(D and E) High levels of the BCFA isovaleric acid (D) and the indole IAA (E) are associated with shorter PFS. Cutoffs in (C)–(E) were determined using maximally selected rank statistics and are annotated below. All *p* values reported correspond to two-sided log-rank tests, and hazard ratios were estimated from Cox proportional hazards models.



(legend on next page)

acid—consistent with patient data but in contrast to *in vitro* data—led to rapid tumor progression compared with carrier-supplemented mice despite enhanced CAR-T cell expansion (Figures 5B–5D).

Following gavage, only ICA was elevated in stool, but all metabolites were robustly increased in portal vein blood and, to a lesser extent, in heart blood, reaching concentrations comparable to those used *in vitro* (Figures 5E–5G). We thereby confirmed that oral gavage increases metabolite levels *in vivo* in compartments where CAR-T cells circulate.

In light of the discrepancy in the effects of BCFA and SCFA, we conducted serial bioluminescence-based proliferation assays on $CD19^+$ A20 cells treated with valeric, isovaleric acid, or ICA *in vitro*. Isovaleric acid-treated A20 cells showed increased proliferation compared with carrier-treated A20 cells, while cells treated with the other metabolites did not (Figure S9A), highlighting a potential direct cancer-promoting effect of isovaleric acid. To further confirm this finding, we supplemented A20-bearing mice with either carrier, valeric, or isovaleric acid or ICA and found increased disease progression (Figures S9B and S9C) and higher tumor burden 10 days after cancer cell injection (Figure S9B) in isovaleric acid-supplemented mice. To further mechanistically validate this finding, we performed bulk RNA sequencing (RNA-seq) on A20 cells treated with either carrier, valeric, or isovaleric acid: principal-component analysis revealed that metabolite treatment was the dominant source of variation between carrier, valeric, and isovaleric acid (Figure S9D), with enriched Gene Ontology (GO) terms substantially overlapping in metabolite-treated cells (Figure S9E). Differential gene expression analysis between valeric and isovaleric acid revealed upregulation of the anti-apoptotic gene *Mcl1* in isovaleric acid-treated A20 cells (Figure S9F), a key gene for carcinogenesis in follicular lymphoma. A semantic space map analysis of enriched GO terms revealed upregulation of cell-cycle regulation and amino acid metabolic processes in valeric acid-treated samples, whereas isovaleric acid upregulated regulation of immune responses, including *Cd274* (PD-L1) among the defining genes of this semantic cluster (Figure S9G). We further confirmed this finding by flow cytometry analysis: treatment with isovaleric acid upregulated MCL-1 and PD-L1 compared with valeric acid (Figure S9H). These data suggest that valeric and isovaleric acid exhibit—despite widely overlapping effects—profound differences in key genes and pathways in carcinogenesis, cell-cycle regulation, metabolism, and immune evasion.

Accordingly, when CAR-T cells were pretreated with isovaleric acid, which excludes confounding effects on tumor cells directly, they exhibited enhanced efficacy comparable to valeric acid (Figures S10A–S10D). Furthermore, the detrimental effect of isovaleric acid gavage could be replicated in an immunocompromised non-obese diabetic (NOD) xenograft gamma (NXG) model, where gavage with isovaleric acid enhanced tumor burden and reduced survival of NALM-6 lymphoma engrafted mice treated with human anti-CD19 CAR-T cells (Figures S11A–S11D).

Additionally, we assessed whether the effects of ICA on human CAR-T cells *in vivo* were AHR-dependent. Therefore, we performed gavage of ICA or carrier in NXG mice engrafted with NALM-6 lymphoma cells and treated with AHR-proficient or AHR-deficient CAR-T cells. Indeed, AHR-deficient CAR-T cells were not inhibited by ICA gavage, while AHR-proficient ones were, confirming a direct dependency of the ICA effect on the CAR-T cell AHR receptor (Figures S12A–S12E).

In summary, we functionally validated the detrimental effects of ICA and isovaleric acid and the beneficial effect of valeric acid on *in vivo* CAR-T cell therapy. Notably, isovaleric acid directly promotes cancer progression despite its favorable effects on CAR-T cells, which can be mitigated by pretreating CAR-T cells before infusion.

A metabolite risk score comprising indole and BCFA and SCFA levels predicts CAR-T cell survival

We finally combined fecal levels of the preclinically validated IMMs valeric acid, isovaleric acid, IAA, and ICA to a 4-parameter risk score, with 1 point assigned for valeric acid below the predefined threshold from our previous analysis (Figure 2) and 1 point for the other metabolites above the threshold. Patients with a risk score of 4 (compared with patients with a risk score ≤ 3) had a significantly reduced PFS ($p < 0.0001$, HR = 2.9; Figure 6A) and reduced OS ($p = 0.0654$, HR = 2; Figure 6B). When adjusted for the potential confounders center, CAR-T costimulatory domain, disease type, antibiotic exposure, CRS grade, sample timing, sex, age, lactate dehydrogenase (LDH), and Eastern Cooperative Oncology Group performance status (ECOG) in a multivariate Cox regression, the fecal risk score remained a strong predictor for PFS and OS (Figures 6C and 6D). Furthermore, using the cut point derived from the entire cohort, we stratified patients within each center individually. The metabolite risk score showed significant associations (univariate

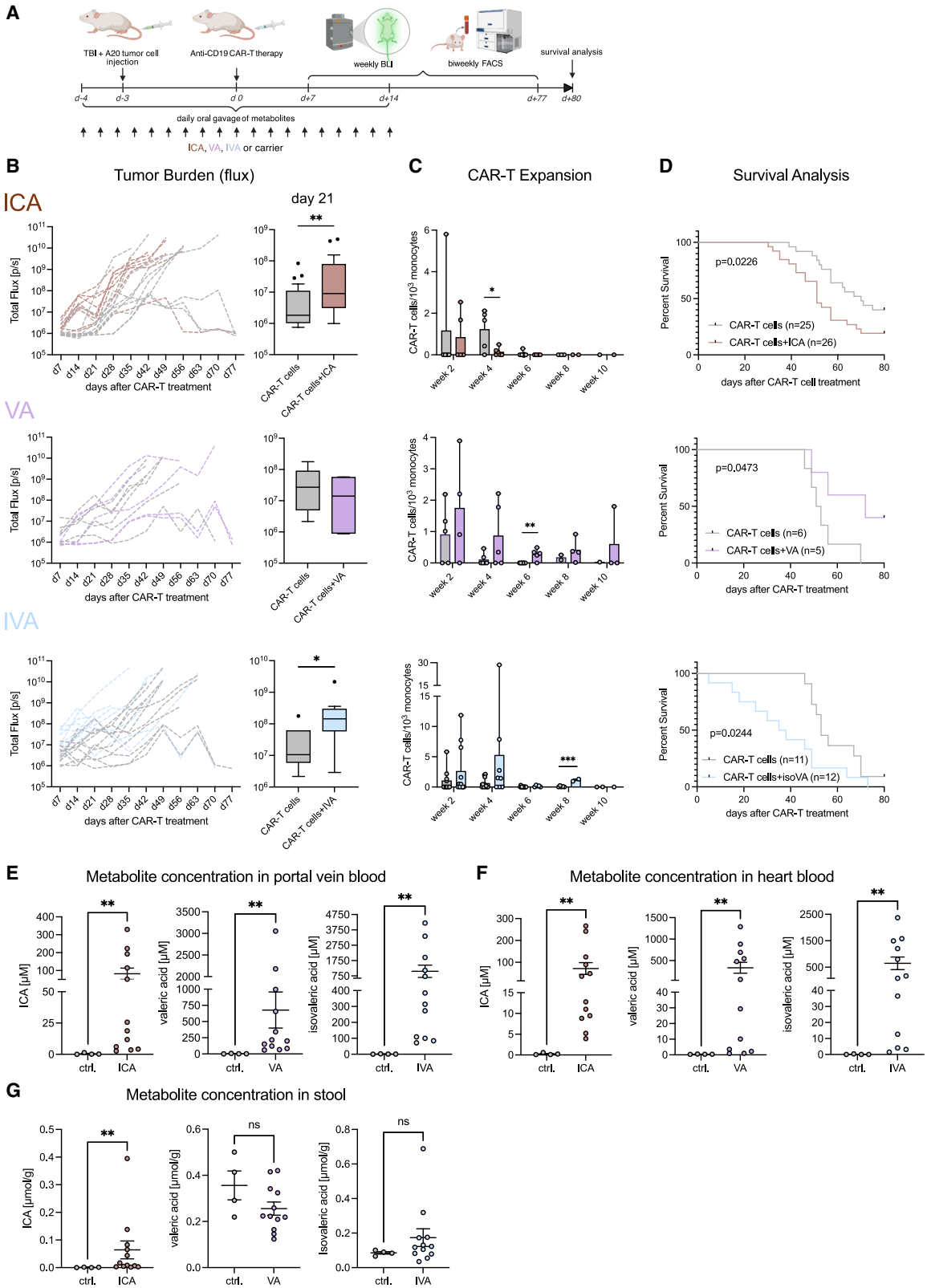
Figure 4. IMMs alter CAR-T cell activity *in vitro*

(A) Anti-HER2 CAR-T cells were activated with HER2 protein in the presence of IAA or ICA ($n = 9$) and valeric and isovaleric acids ($n = 9$ and 6) before analysis via flow cytometry. The plots show the relative (%) change of T cell markers of donor-matched metabolite-treated relative to carrier-treated $CD8^+$ and $CD4^+$ CAR-T cells. MFI: median fluorescence intensity.

(B) Anti-human HER2 and anti-human CD19 CAR-T cells were incubated with ICA, IAA ($n = 4$ for HER2 and $n = 6$ for CD19), valeric or isovaleric acid ($n = 8$ for HER2 and $n = 13$ for CD19), and co-cultured with $HER2^+$ SKOV3 and $CD19^+$ NALM-6 cells, respectively, in a bioluminescence cell killing assay.

(C) Plots of single cells in uniform manifold approximation and projection (UMAP) space with annotation from scRNA-seq of anti-HER2 CAR-T cells, split by treatment. Anti-HER2 CAR-T cells from four donors were co-cultured with the metabolites ICA, isovaleric acid, valeric acid, or a carrier control and analyzed via scRNA-seq. Black circles mark clusters that are most prominently changing after the respective treatment.

(D) Barplots of gene set enrichment analysis (GSEA) results from the scRNA-seq experiment described in (C) show selected pathways/gene sets for CD4 and CD8 cells and different treatment conditions (vs. carrier control). The sign indicates the direction of the regulation (up, positive; down, negative). Tukey-style boxplots in (A) and (B). $^*p < 0.05$, $^{**}p < 0.01$, $^{***}p < 0.001$, $^{****}p < 0.0001$ from a two-sided donor-matched paired Student's t test. Colors in (C) reflect the annotation of T cell subtypes/states. CD8 subtypes were not annotated in more detail due to small population size. The size of the bars in (D) corresponds to the normalized enrichment score (NES). The bars are colored by the −log10 of the q value (false discovery rate [FDR]); values are clipped at −3 and 3 to improve visibility.
See also Figures S5–S8.



(legend on next page)

Cox proportional hazards [PH] model) with PFS in two of the three centers (Heidelberg: $p = 0.024$, HR = 3 [1.1–8]; Regensburg: $p = 0.0074$, HR = 2.5 [1.3–5]), with a trend in the third center (Munich: $p = 0.16$, HR = 4.8 [0.44–54]), which had limited sample size ($n = 10$; Figure S13A). Additionally, the risk score remained predictive among the most prevalent subgroups in this study, including patients with CD19-CAR-T, $CD19^+$ NHL, DLBCL, and MM (Figures S13B–S13E).

Of note, a similar risk score based on serum levels of valeric acid, isovaleric acid, and IAA (ICA was omitted due to low serum levels) was also associated with poorer PFS ($p = 0.00201$, HR = 3.6; Figure S14A) and OS ($p = 0.000466$, HR = 5; Figure S14B). However, this serum-based risk score demonstrated a lower discriminatory performance as reflected by the loss of significant association with PFS and OS in a multivariate Cox regression model as well as reduced AUC in both ROC and precision recall analyses compared with the fecal risk score (0.668 and 0.667 [fecal] vs. 0.594 and 0.647 [serum]; Figures S14C and S14D). This suggests that fecal metabolite levels may be more informative for survival after CAR-T cell therapy than serum levels.

DISCUSSION

In this study, we outline the ambivalent role of gut IMMs on CAR-T cell therapy. We could reproduce previous findings suggesting a negative role of antibiotics prior to CAR-T infusion on therapeutic outcomes.[8,9,11]

Antibiotics were associated with reduced bacterial richness, diversity, and fecal SCFAs and BCFAs, while richness and diversity served as a weaker predictor of CAR-T cell outcomes compared with antibiotics alone. We investigated the association of single bacteria and bacterial genera on therapeutic outcomes unbiased solely based on data from our study with various bioinformatic tools and found next to no overlap between the different tools when analyzing PFS, OS, and CR rates at day 180. Additionally, we specifically tested microbial species and genera associated with CAR-T cell outcomes in other studies.[9,10,13,18,22] Thereby, only the strictly anaerobic *B. longum* previously identified by Stein-Thoeringer et al.[8] was associated with improved PFS and OS. *B. longum* was positively associated with SCFAs in the feces of patients, including valeric acid, but not with isovaleric acid, ICA, and IAA. Although we could reproduce anecdotal evidence implicating this single strain, individual bacterial species do not appear to predict CAR-T cell outcomes in our cohort. Even when considering only the direction of reported effects, we found no alignment with outcomes in our dataset.[9–11,22] While larger studies with increased patient numbers may enable the robust identification of microbial taxonomic signatures, functional and metabolic profiles are likely to provide more consistent and informative insights into the microbiome's influence on CAR-T cell therapy outcomes.

Interestingly, aerobic and anaerobic metabolism pathways show opposing associations with PFS. The overgrowth of facultative anaerobes and strict aerobes in the gut has been recognized as a major driver of dysbiosis and has been shown to detrimentally affect immunotherapy.[23–25] Thereby, we speculate that microbial immunomodulatory metabolic output might directly affect CAR-T cell outcomes. It is noteworthy that most gut IMMs, including SCFAs and secondary bile acids, are produced as key metabolic products by anaerobic commensals.[26]

Unsupervised hierarchical clustering of fecal microbial metabolites showed that a loss of IMMs was associated with poorer outcomes and lower CR rates compared with patients proficient in IMM. However, within the IMM-proficient group, a fraction with upregulation of BCFAs and indoles experienced intermediate response rates and PFS.

The association of single IMMs with PFS not only revealed a positive association of fecal SCFAs—including acetic, propionic, and valeric acid—with both PFS and OS but also a negative association of indole derivatives (ICA and IAA) and BCFAs—namely isobutyric acid, 2-methylbutyric acid, and isovaleric acid—with PFS, suggesting an ambivalent role of these IMMs in CAR-T cell outcomes. We and others have previously investigated the mechanism of action of valeric acid on CAR-T cells and demonstrated improvement of CAR-T cell metabolism and fitness by inhibiting histone deacetylases and fueling the citric acid cycle.[11,13,14] However, less is known for indole derivatives and BCFAs in the context of CAR-T cell therapy.

In vitro investigations demonstrated a direct immunomodulatory effect of these IMMs. Valeric acid (as previously described[11,13,14]) and isovaleric acid enhanced CAR-T cell lysis, effector-marker expression, and metabolic fitness, whereas ICA and IAA impaired cell lysis and effector-marker expression. scRNA-seq further revealed upregulation of the cellular receptor for indoles, the AHR[19,20] pathway, alongside a downregulation of T cell activating pathways for ICA. Opposingly, valeric and isovaleric acid induced T cell activating and metabolic pathways.

Figure 5. ICA and IVA supplementation impair and VA supplementation improves CAR-T cell efficacy

(A) Syngeneic $CD19^+$ A20 lymphoma-bearing mice were orally gavaged with either ICA, valeric acid (VA), isovaleric acid (IVA), or carrier.

(B) Tumor burden with total flux of bioluminescent imaging and quantitative comparison on day 21 after A20 cell injection. ICA total flux shows one representative experiment with $n = 10$, whereas quantitative comparison on day 21 shows pooled data from three independent experiments ($n = 25–26$).

(C) CAR-T cell expansion in blood as CAR-T cells per 10^5 monocytes. For ICA, one representative experiment is shown ($n = 5–6$).

(D) Survival analysis plotted as percent survival followed for 80 days after CAR-T cell treatment. ICA shows pooled data from three independent experiments ($n = 25–26$).

(E–G) BALB/c mice received oral gavage of a metabolite cocktail consisting of VA, IVA, and ICA, or carrier control. A total of $n = 12$ mice received the metabolite cocktail, whereas $n = 4$ mice received the carrier control. Thirty minutes post-gavage, (E) portal vein blood, (F) heart blood, and (G) stool were collected, and metabolite concentrations were quantified by mass spectrometry. Tukey-style boxplots in (B). Bar graph in (C) shows the mean with the range of mice present at the indicated time points. Scatterplots in (E)–(G) show the mean with the standard error of the mean. Significance in boxplots in (B) and bar graphs in (C) was determined by two-sided unpaired Student's *t* test, in Kaplan-Meier curves (D) with two-sided log-rank (Mantel-Cox) test, and in scatterplots (E)–(G) by Mann-Whitney U test. $^*p < 0.05$, $^{**}p < 0.01$. Numbers of mice for valeric and IVA in (B) and (C) are as indicated in the survival analysis chart in (D).

See also Figures S9–S12.

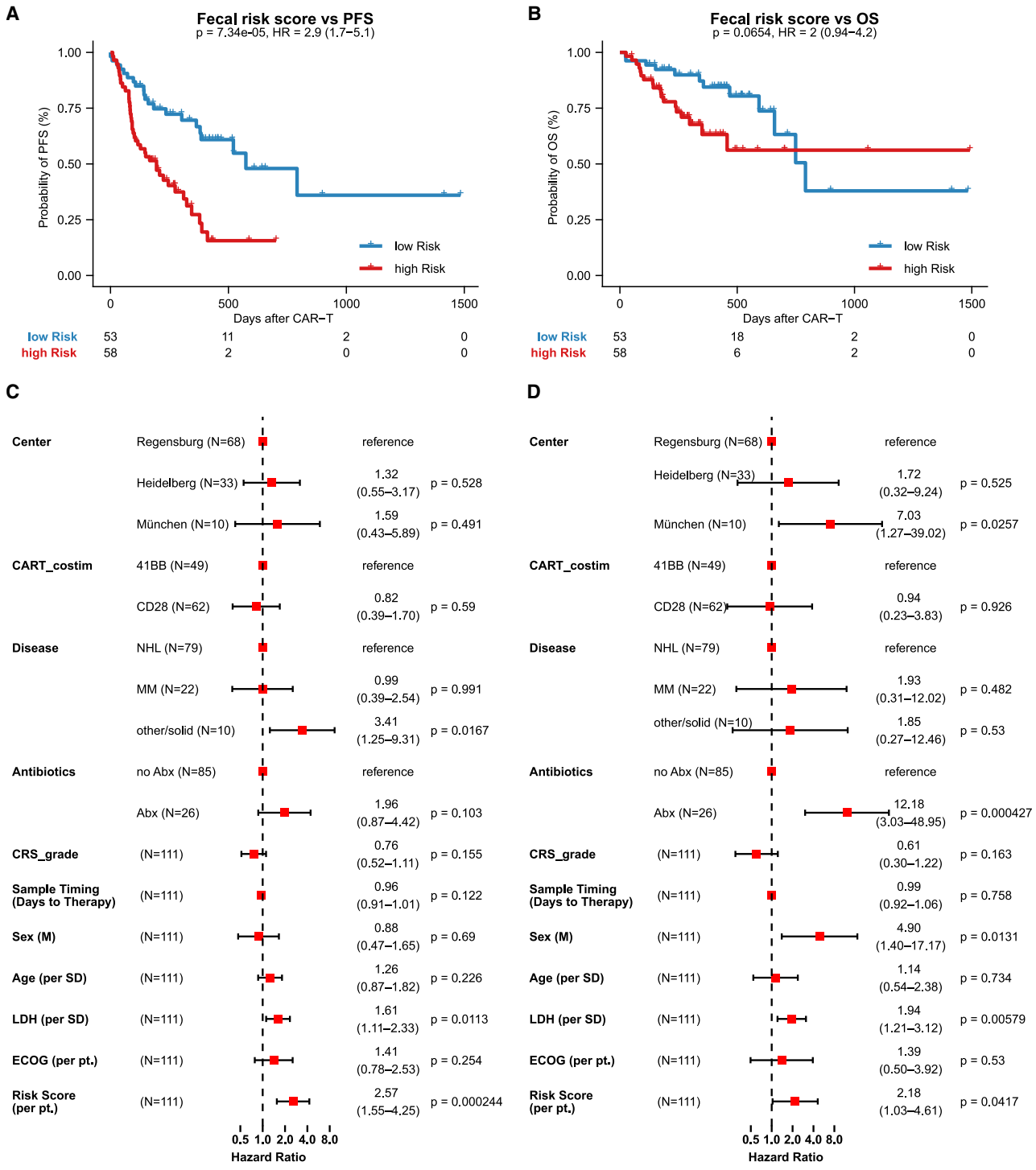


Figure 6. A four-parameter fecal risk index comprising VA, IVA, IAA, and ICA is predictive for CAR-T cell survival

(A and B) Kaplan-Meier analysis revealed that the fecal risk score significantly stratified patients by PFS (patients scoring 4 vs. ≤3) (A) and OS (B).

(C and D) These associations remained statistically robust after adjustment for the possible confounders in multivariate Cox proportional hazards models. All *p* values for survival analysis in (A) and (B) correspond to two-sided log-rank tests. Hazard ratios and 95% confidence intervals in (A)–(D) were estimated using Cox proportional hazards regression models. *p* values for individual predictors in the multivariate Cox model in (C) and (D) were obtained from two-sided Wald tests. See also Figures S13 and S14.

Thereby, SCENITH analysis confirmed higher protein translation and lower glucose dependence for valeric and isovaleric acid-treated CAR-T cells in line with our previous results.[13,14] Mechanistically, valeric and isovaleric acid increase metabolic activity (as evidenced by activation of the mTOR/S6 pathway) and induce a multifuel program with reduced glucose dependence and increased fatty acid and amino acid oxidation. Furthermore, valeric and isovaleric acid served as potent and direct HDAC2 inhibitors in T cells. Genetic deletion of *AHR* mitigated the detrimental effects of ICA *in vitro* and *in vivo*, confirming an AHR-dependent mode of action.

In an immunocompetent murine model of anti-murine CD19 CAR-T therapy, oral supplementation with ICA impaired CAR-T cell function and reduced CAR-T cell numbers, whereas valeric acid improved expansion, reduced tumor burden, and improved survival. The deleterious effect of isovaleric acid on CAR-T cell efficacy *in vivo*, despite enhancing *in vitro* function, seems paradoxical but is explained by tumor-intrinsic effects: upregulation of anti-apoptotic MCL-1 and immune-evasive PD-L1 and promotion of tumor cell growth *in vitro* and *in vivo*. These findings were validated in an immunocompromised NXG model of NALM6-lymphoma. Consistent with this, isovaleric acid has been linked to colorectal cancer progression and to downregulation of pro-inflammatory pathways such as nuclear factor κB (NF-κB) and NLRP3,[27–29] which are known to influence T cell-mediated cancer immunity.[30] Conversely, valeric acid improved CAR-T cell efficacy and survival, consistent with clinical observations and *in vitro* models.

Our study demonstrates that not all gut IMMs are advantageous. Indoles were predictive of therapy failure and suppressed CAR-T cell function *in vivo* and *in vitro*, whereas the BCFA isovaleric acid promoted tumor progression independent of CAR-T cells. While the suppressive nature of other tryptophan-derived AHR ligands, such as kynurenine, is widely recognized in cancer immunotherapy, no studies to date have identified a detrimental role for bacterial tryptophan metabolites.[31–35] By contrast, other members of the indole family, such as IPA, have been described as enhancers of cancer immunotherapy.[18] This effect has—among other mechanisms—been attributed to HDAC inhibition; however, the relative contribution of the indole backbone vs. the SCFA substituent propionic acid has not yet been explored.[36–38] Indeed, in our cohort we found a weakly positive association of IPA with CAR-T cell outcomes. Additionally, ICA was described as a facilitator of $CD8^+$ T cell function in ICI when released by an intratumoral microbe.[39] These findings indicate that microbial co-stimulation can work synergistically with the released metabolite, potentially offsetting immunosuppressive effects of the metabolite alone. Additionally, while some studies report that AHR activation reduces T cell-mediated defense against influenza A[40–42] others find that it enhances tissue-resident T cell function and facilitates cancer clearance.[39,43] We assume that these differences arise from different localizations, contexts (single metabolites or microbially delivered metabolites), and differentiation programs.

While SCFAs are produced solely in fermentative processes by anaerobic bacteria, indoles have a wider variety of sources, including aerobic and aerotolerant microbes.[19,20,44,45] Notably, patients with antibiotic therapy only showed remotely different levels of fecal indoles. We thereby speculate that the differential indole-producing strains are affected differently during antibiotic therapy and ID compared with the fermentative anaerobes producing SCFAs. This may, in part, explain the independent predictive value of indoles for dismal outcomes.

CAR-T cell therapy involves the adoptive transfer of live T cells, unlike ICI, which primarily re-arms tissue-resident T cells. Unlike antibody-based immunotherapies, adoptive T cell transfer requires an initial homing phase to lymphoid organs. Studies in lymphodepleted mice have shown that the primary homing targets are connected to the gut or portal venous system: the spleen, liver, and mesenteric lymph nodes. This implicates that adoptively transferred T cells encounter metabolites largely absent from serum due to their first-pass effect.[45–47] We speculate that priming during this early homing and engraftment phase with gut IMMs is crucial for therapeutic efficacy. Inducing the AHR-driven transcriptional and differentiation program via indoles or enhancing the metabolic and epigenetic fitness of CAR-T cells via valeric acid in this phase may be critical for antitumor activity. This early conditioning in lymphoid organs may explain why antibiotics administered prior to—but not after—CAR-T cell infusion consistently impair therapy efficacy throughout different cohorts.[8,9,11]

In summary, we identified IMMs associated with both beneficial and detrimental clinical outcomes following CAR-T cell therapy. Some of these effects can be explained by direct immunomodulation of CAR-T cells and are consistent across patients, *in vitro* studies, and preclinical *in vivo* models—such as the beneficial effect of valeric acid and the detrimental effect of ICA. Others, such as isovaleric acid, display negative associations in patients and preclinical *in vivo* models but enhance CAR-T cell function *in vitro* and CAR-T cell expansion *in vivo*, underscoring the underlying complexity. In contrast to approaches focusing on single bacterial species, our research led to a biologically validated clinical risk score for fecal IMMs that integrates valeric acid, isovaleric acid, ICA, and IAA and demonstrates high accuracy in predicting CAR-T cell therapy outcomes.

Limitations of the study

Of note, our study has important limitations. Although we elucidated how isovaleric acid shapes cancer cells, the tumor microenvironment, and ultimately CAR-T cell function, our observations open new avenues for IMM research that warrant follow-up investigations. Additionally, although we included a relatively large patient cohort and stratified analyses, certain CAR-T cell indications, such as solid tumors, are rare, precluding individual analyses and robust conclusions. Moreover, we only focused on the sampling time point prior to CAR-T cell therapy to find potential biomarkers to allow predictions prior to CAR-T cell infusion. We further acknowledge that larger and independent cohorts will be needed to fully define disease- or product-specific metabolic signatures in disease types or products that were not represented in high numbers in this study and to determine whether refinement of the risk score for specific indications could improve predictive performance.

Conclusions

Our research reveals an ambivalent role for the microbiome and IMMs, demonstrating that specific metabolites impair CAR-T cell

function while others enhance their therapeutic efficacy. Future interventional strategies can leverage these findings by designing precision fecal microbiome transfer products based on metabolic pathways and metabolite profiles. Accordingly, microbial consortia—either in their natural form or engineered to express specific pathways—can be utilized as live biotherapeutic products to achieve this goal in patients with a high metabolite risk score. Our study challenges the concept of a "healthy" microbiome defined solely by taxonomy and emphasizes the importance of microbial pathways and metabolism in shaping the human immune system rather than individual species. In this context, rather than taxonomic features, microbial pathways and metabolites could serve as universal biomarkers of a healthy microbiome state.[25,48]

RESOURCE AVAILABILITY

Lead contact

Requests for further information and resources should be directed to and will be fulfilled by the lead contact, Hendrik Poeck (hendrik.poeck@ukr.de).

Materials availability

The cell line generated during this study is available upon request.

Data and code availability

- The scRNA-seq data generated in this study have been deposited at the European Genome-Phenome Archive (EGA). The accession numbers are EGA: EGAS50000001386 (study) and EGA: EGAD50000002012 (dataset). They are available upon request if conditions of the data access agreement linked to the dataset are met. Access can be requested via the website of the dataset at EGA.
- The host decontaminated metagenomic sequencing data obtained in this study have been deposited at the European Nucleotide Archive (ENA) as ENA: PRJEB101146 and are publicly available as of the date of publication.
- The bulk RNA-seq data generated in this study have been deposited at Gene Expression Omnibus (GEO) as GEO: GSE329624 and are publicly available as of the date of publication.
- Human mass spectometry data have been deposited at MassIVE as MassIVE: MSV000101883 and at Zenodo under https://doi.org/10.5281/zenodo.17475484. They are publicly available as of the date of publication.
- Mouse mass spectometry data have been deposited at MassIVE as MassIVE: MSV000101884 and at Zenodo under https://doi.org/10.5281/zenodo.20085233. They are publicly available as of the date of publication.
- Clinical data and associated features are available from the lead author upon reasonable request, in accordance with the German (GPDR) and European data protection regulations.
- All original code used to analyze metagenomics and metabolomics data in this study is available on GitHub at https://github.com/lit-regensburg/IMM-CART-Paper_MGX-MBX.
- All original code used to analyze scRNA-seq data is available at https://github.com/lit-regensburg/scRNA_CAR_T_metabolites.
- All original code used to analyze bulk RNA-seq data is available at https://github.com/lit-regensburg/IMM-CART-Paper_RNASeq-A20
- Any additional information required to reanalyze the data reported in this paper is available from the lead contact upon reasonable request.

ACKNOWLEDGMENTS

We would like to thank Maria Krieger, Eva Herschberger, and Christian Schreiber for excellent technical assistance. Sequencing experiments were conducted at the NGS & Data Technologies Core Unit of the Leibniz Institute of Immunotherapy (LIT), Germany (https://lit.eu/facilities/ngs-and-data-technologies). We would like to thank Hanna Stanewsky for her assistance with the scRNA-seq experiment. Flow cytometry experiments were conducted at the Flow Cytometry Core Unit of the Leibniz Institute of Immunotherapy (LIT), Germany. We would like to thank Petra Hofmann and her team for their assistance. The Sciex QTrap 6500+ mass spectrometer was funded in part by the German Research Foundation (DFG-INST 95/1873-1 FUGG).

This study was supported by the German Research Foundation (Deutsche Forschungsgemeinschaft, DFG; project no. 395357507 – SFB 1371 to H.P. and M. Schirmer and DFG project no. 324392634-TRR 221 to H.P. and W.H.), DFG PO 1575/5-1 (to H.P.), the German Cancer Aid (70114547 to H.P.), the Wilhelm Sander Foundation (2021.040.1 to H.P.), and the Reform program of the University of Regensburg (to M.P.). H.P. is supported by the EMBO Young Investigator Program and the Bavarian Cancer Research Center (BZKF) (to M.P., M.A.F., M.H., M.L., and H.P.). This work was funded/co-funded by the European Union (project MICROBOTS, grant no. 101124680 to H.P.). Views and opinions expressed are, however, those of the author(s) only and do not necessarily reflect those of the European Union or the European Research Council. Neither the European Union nor the granting authority can be held responsible for them. M.P.T. is supported by the Monika Kutzner Foundation and the European Research Council (MSCA fellowship 101106951). J.S. reports funding from an NIH/NIAID DP2 Grant DP2AI164318, an NCI R01 Grant R01CA269617, and a Gabrielle's Angel Foundation Grant. Support was received from the Innovative Medicines Initiative 2 Joint Undertaking, the European Union's Horizon 2020 research and innovation program, the EFPIA and the European Hematology Association (EHA) (grant agreement no. 945393, T2EVOLVE; HORIZON-HLTH-2025-01-TOOL-01 project CARDIO to M.H. and M.L.), the Wilhelm Sander Foundation (grant no. 2022.134.1 to K.Z.M. and M.L.), the ERA-NET TRANSCAN-3 (EC co-funded call 2021, SmartCAR-T to K.Z.M., M.H., and M.L.), the Paula & Rodger Riney Foundation (to M.H. and M.L.), IZKF Würzburg (S-511, C-543 to M.L.), and the DFG (TRR 221 [subproject A03 and A06 to M.H. and M.L.; subproject A08 to H.P. and M.P.], CRC1525 [subproject C06 to M.L.], and SFB-TRR 338/3 2026–452881907 [subproject A02; to M.H. and subproject C04 to M.L.]). This work was performed in the framework of the National Cancer Therapy Center (NCT) WERA and the Bavarian Cancer Research Center (BZKF). The graphical abstract and Figures 1A, 4A, 4B, 5A, S5A, S7A, S10A, S11A, and S12A were created with BioRender.com.

AUTHOR CONTRIBUTIONS

M.P., S.G., D.S., S.H., E.T.O., and H.P. wrote the original draft. M.P., S.G., D.S., S.H., L.B., M.T., P.M., S.D., G.L.-G., J.N.S., S. Göttert, K.H., P.H., K.G.K., C.G., M.P.T., J.D., S. Sameri, K.Z.-M., S. Staudt, A.G., T.W., K.N., T.Z., D.M.C.D.S., S.T., M. Schirmer, K.K., J.S., M. Schmitt, M.F., C.H.-L., J.B., L.G., M.R., M.H., C.B., L.Z., M. Subklewe, V.B., M.-L.S., C.S.-T., M.L., S.K., M.A.F., E.T.O., and H.P. contributed to methodology. M.P., M.-L.S., C.S.-T., M.L., S.K., M.A.F., and H.P. acquired funding. M.P., S.G., D.S., S.H., L.B., M.T., P.M., S.D., J.N.S., S. Göttert, K.H., P.H., C.G., M.P.T., J.D., S. Sameri, D.C.H., K.Z.-M., S. Staudt, K.N., T.Z., K.K., C.H.-L., and J.B. performed experiments. M.P., K.G.K., W.H., D.C.H., L.H., M.E., D. Wolff, D. Weber, E.M., A.D., M. Schmitt, M. Subklewe, V.B., M.-L.S., C.S.-T., M.A.F., and H.P. curated clinical data and recruited patients. M.P., S.G., W.H., M.E., D. Wolff, M. Schmitt, M.F., L.G., M.R., M.H., C.B., L.Z., M. Subklewe, V.B., M.-L.S., C.S.-T., M.L., S.K., M.A.F., E.T.O., and H.P. supervised the study. All authors read, edited, and approved the article.

DECLARATION OF INTERESTS

M.P. received speaker's honoraria and travel funds from Amgen, Kite, and Takeda. M.L. and M.H. are listed as inventors on patent application WO2021/058811A1. M.H. is listed as an inventor on patent applications and granted patents related to CAR-T technologies that have been filed by the Fred Hutchinson Cancer Research Center, Seattle, WA, and by the University of Würzburg, Würzburg, Germany. M.H. is a co-founder and equity owner of TCURX GmbH, Würzburg, Germany. M.H. received honoraria from Celgene/BMS, Janssen, and Kite/Gilead. J.S. is co-founder of Postbiotics Plus

Research and holds equity. J.S. serves on an advisory board and holds equity of Jona Health. J.S. has filed intellectual property applications related to the microbiome (reference number #63/299,607). D.W. received research support from Novartis and honoraria from Novartis, Behring, Incyte, Sanofi, and Neovii, Therakos. D.M.C.D.S. received research funding from Regeneron. S.T. received honoraria from Johnson & Johnson, BMS, GSK, Amgen, Pfizer, Stemline, Oncopeptides, Sanofi, and Kyowa Kirin. S.T. reports consultancy in Takeda, Oncopeptides, and Menarini-Stemline. M.A.F. received honoraria from Sanofi and Novartis and travel support from Sanofi. S.K. reports grants and personal fees from Plectonic and TCR2 Inc. S.K. reports personal fees from Cymab, Miltenyi Biomedicines, Bristol Myers Squibb, GSK, Galapagos, and Novartis and grants from Catalym and Arcus Biosciences outside the submitted work as well as a patent for EP3310805B1 issued and licensed to TCR2 Inc. and a patent for EP3362569B1 issued and licensed to Carina Biotech. L.H. is a part of the advisory committee of Bristol Myers Squibb, Gilead, Johnson & Johnson, Pierre Fabre, and Sanofi. L.H. has travel support from Amgen, Gilead, and Johnson & Johnson. M.K. has consultancy roles in AstraZeneca, Takeda, Kyverna, Amgen, Miltenyi, Gilead/Kite, Orbital, Aculeus, AvenCell, Autolus, Crossbow, and Caribou. M.K. received honoraria from Molecular Partners, AbbVie, Advesya, Roche, and Seagen. M.R.M.v.d.B. has received research support and stock options from Seres Therapeutics and stock options from Notch Therapeutics and Pluto Therapeutics; he has received royalties from Wolters Kluwer; has consulted and received honoraria from or participated in advisory boards for Seres Therapeutics, Vor Biopharma, Rheos Medicines, Frazier Healthcare Partners, Nektar Therapeutics, Notch Therapeutics, Ceramedix, Lygenesis, Pluto Therapeutics, GlaxoSmithKline, Da Volterra, Thymofox, Garuda, Novartis (spouse), Synthekine (spouse), Beigene (spouse), and Kite (spouse); he has IP licensing with Seres Therapeutics and Juno Therapeutics; and holds a fiduciary role on the Foundation Board of DKMS (a nonprofit organization). L.Z. is a founder of everImmune and serves as President of the everImmune Scientific Advisory Board; L.Z. has received honoraria from everImmune. L.Z. has a research contract with Daiichi Sankyo. L.Z. is an employee of Gustave Roussy and Faculté de Médecine Paris XI. L.Z. was previously Editor-in-Chief of OncoImmunology. L.Z. previously served on scientific advisory boards for EpiVax, Lytix Biopharma, Tusk Therapeutics, Hookipa, and IHU Méditerranée Infections (as President of the SAB). L.Z. previously served on the Board of Directors of Transgene. Past research contracts included Biomérieux, Kaleido, Elior, Carrefour, Merus, Roche, Tusk, Pileje, Incyte, Bristol Myers Squibb, GlaxoSmithKline, Lytix Biopharma, Innate Pharma, Transgene, and 9 Meters. L.Z. also had a former teaching contract with Pierre Fabre.

DECLARATION OF GENERATIVE AI AND AI-ASSISTED TECHNOLOGIES IN THE WRITING PROCESS

During the preparation of this work, the authors used ChatGPT and Perplexity AI to refine sentence formulations and improve manuscript clarity. After using these tools, the authors reviewed and edited the content as needed and take full responsibility for the content of the published article.

STAR★METHODS

Detailed methods are provided in the online version of this paper and include the following:

- KEY RESOURCES TABLE
- EXPERIMENTAL MODEL AND STUDY PARTICIPANT DETAILS
  - Human Participants
  - Cell lines
  - Experimental animals
- METHOD DETAILS
  - Sample collection
  - Mass spectrometry-based quantitation of metabolite levels
  - Human T cell isolation and activation
  - Murine T cell and blood isolation
  - Lentivirus production
  - Lentiviral human T cell transduction
  - Retroviral human T cell transduction
  - Murine CAR-T cell production
  - Cas9 ribonucleoprotein-based gene editing
  - IMM handling, dilution, carrier control and dosing
  - Cell lysis assays
  - Protein-based CAR-T cell stimulation and flow cytometry
  - Single-cell RNA sequencing (scRNA-seq) with 10x Genomics GEM-X
  - scRNA-seq raw read processing
  - scRNA-seq data analysis
  - Bulk RNA sequencing (bulk RNA-seq)
  - CAR-T cell proliferation assay
  - SCENITH assay of artificially stimulated anti-HER2 CAR-T cells
  - Immuno-Western Blot
  - HDAC2 Inhibition Assay
  - Bioluminescence-based proliferation assay
  - Animal experiments
  - Metabolite Bioavailability Assay
  - Metagenomic Sequencing
  - Plotting and Statistics
  - Survival Curves
  - Metagenomic Data Analysis
  - Metabolite Data Analysis
  - Bulk RNA-seq Data Analysis
  - Risk Score
- QUANTIFICATION AND STATISTICAL ANALYSIS

SUPPLEMENTAL INFORMATION

Supplemental information can be found online at https://doi.org/10.1016/j.cell.2026.09.004.

Received: December 22, 2025
Revised: May 22, 2026
Accepted: September 2, 2026
Published: September 28, 2026

REFERENCES

1. Munshi, N.C., Anderson, L.D., Shah, N., Madduri, D., Berdeja, J., Lonial, S., Raje, N., Lin, Y., Siegel, D., Oriol, A., et al. (2021). Idecabtagene Vicleucel in Relapsed and Refractory Multiple Myeloma. N. Engl. J. Med. *384*, 705–716. https://doi.org/10.1056/NEJMoa2024850.
2. Locke, F.L., Miklos, D.B., Jacobson, C.A., Perales, M.-A., Kersten, M.-J., Oluwole, O.O., Ghobadi, A., Rapoport, A.P., McGuirk, J., Pagel, J.M., et al. (2022). Axicabtagene Ciloleucel as Second-Line Therapy for Large B-Cell Lymphoma. N. Engl. J. Med. *386*, 640–654. https://doi.org/10.1056/NEJMoa2116133.
3. Berdeja, J.G., Madduri, D., Usmani, S.Z., Jakubowiak, A., Agha, M., Cohen, A.D., Stewart, A.K., Hari, P., Htut, M., Lesokhin, A., et al. (2021). Ciltacabtagene autoleucel, a B-cell maturation antigen-directed chimeric antigen receptor T-cell therapy in patients with relapsed or refractory multiple myeloma (CARTITUDE-1): a phase 1b/2 open-label study. Lancet *398*, 314–324. https://doi.org/10.1016/S0140-6736(21)00933-8.
4. Shah, B.D., Ghobadi, A., Oluwole, O.O., Logan, A.C., Boissel, N., Cassaday, R.D., Leguay, T., Bishop, M.R., Topp, M.S., Tzachanis, D., et al. (2021). KTE-X19 for relapsed or refractory adult B-cell acute lymphoblastic leukaemia: phase 2 results of the single-arm, open-label, multicentre ZUMA-3 study. Lancet *398*, 491–502. https://doi.org/10.1016/S0140-6736(21)01222-8.
5. Belkaid, Y., and Hand, T.W. (2014). Role of the Microbiota in Immunity and Inflammation. Cell *157*, 121–141. https://doi.org/10.1016/j.cell.2014.03.011.
6. Honda, K., and Littman, D.R. (2016). The microbiota in adaptive immune homeostasis and disease. Nature *535*, 75–84. https://doi.org/10.1038/nature18848.

7. Routy, B., Le Chatelier, E., Derosa, L., Duong, C.P.M., Alou, M.T., Daillère, R., Fluckiger, A., Messaoudene, M., Rauber, C., Roberti, M.P., et al. (2018). Gut microbiome influences efficacy of PD-1–based immunotherapy against epithelial tumors. Science *359*, 91–97. https://doi.org/10.1126/science.aan3706.

8. Stein-Thoeringer, C.K., Saini, N.Y., Zamir, E., Blumenberg, V., Schubert, M.-L., Mor, U., Fante, M.A., Schmidt, S., Hayase, E., Hayase, T., et al. (2023). A non-antibiotic-disrupted gut microbiome is associated with clinical responses to CD19-CAR-T cell cancer immunotherapy. Nat. Med. *29*, 906–916. https://doi.org/10.1038/s41591-023-02234-6.

9. Smith, M., Dai, A., Ghilardi, G., Amelsberg, K.V., Devlin, S.M., Pajarillo, R., Slingerland, J.B., Beghi, S., Herrera, P.S., Giardina, P., et al. (2022). Gut microbiome correlates of response and toxicity following anti-CD19 CAR T cell therapy. Nat. Med. *28*, 713–723. https://doi.org/10.1038/s41591-022-01702-9.

10. Hu, Y., Li, J., Ni, F., Yang, Z., Gui, X., Bao, Z., Zhao, H., Wei, G., Wang, Y., Zhang, M., et al. (2022). CAR-T cell therapy-related cytokine release syndrome and therapeutic response is modulated by the gut microbiome in hematologic malignancies. Nat. Commun. *13*, 5313. https://doi.org/10.1038/s41467-022-32960-3.

11. Prasad, R., Rehman, A., Rehman, L., Darbaniyan, F., Blumenberg, V., Schubert, M.-L., Mor, U., Zamir, E., Schmidt, S., Hayase, T., et al. (2025). Antibiotic-induced loss of gut microbiome metabolic output correlates with clinical responses to CAR T-cell therapy. Blood *145*, 823–839. https://doi.org/10.1182/blood.2024025366.

12. Bachem, A., Clarke, M., Kong, G., Tarasova, I., Dryburgh, L., Kosack, L., Lee, A.R., Newland, L.D., Wagner, T., Bawden, E., et al. (2025). Microbiota-derived butyrate promotes a FOXO1-induced stemness program and preserves CD8+ T cell immunity against melanoma. Immunity *58*, 2799–2813.e8. https://doi.org/10.1016/j.immuni.2025.10.004.

13. Luu, M., Riester, Z., Baldrich, A., Reichardt, N., Yuille, S., Busetti, A., Klein, M., Wempe, A., Leister, H., Raifer, H., et al. (2021). Microbial short-chain fatty acids modulate CD8+ T cell responses and improve adoptive immunotherapy for cancer. Nat. Commun. *12*, 4077. https://doi.org/10.1038/s41467-021-24331-1.

14. Staudt, S., Nikolka, F., Perl, M., Franz, J., Leblay, N., Yuan, X.-K., Larrayoz, M., Lozano, T., Warmuth, L., Fante, M.A., et al. (2025). Metabolization of microbial postbiotic pentanoate drives anti-cancer CAR T cells. bioRxiv, 2024.08.19.608538. https://doi.org/10.1101/2024.08.19.608538.

15. Klysz, D.D., Fowler, C., Malipatlolla, M., Stuani, L., Freitas, K.A., Chen, Y., Meier, S., Daniel, B., Sandor, K., Xu, P., et al. (2024). Inosine induces stemness features in CAR-T cells and enhances potency. Cancer Cell *42*, 266–282.e8. https://doi.org/10.1016/j.ccell.2024.01.002.

16. Trefny, M.P., Kroemer, G., Zitvogel, L., and Kobold, S. (2025). Metabolites as agents and targets for cancer immunotherapy. Nat. Rev. Drug Discov. *24*, 764–784. https://doi.org/10.1038/s41573-025-01227-z.

17. Yin, L., Lv, B., Ge, J., Qi, Y., Xia, J., Ma, S., Wang, Y., Liu, Y., Zhou, D., Cao, J., et al. (2025). The impact of antibiotic use on outcomes of relapsed/refractory multiple myeloma patients treated with CAR-T therapy. Front. Immunol. *16*, 1566016. https://doi.org/10.3389/fimmu.2025.1566016.

18. Marcos-Kovandzic, L., Avagliano, M., Ben Khelil, M., Srikanthan, J., Abdallah, R., Petrocelli, V., Rengassamy, J., Alfaro, A., Bied, M., Fidelle, M., et al. (2025). Gut Microbiota Modulation through *Akkermansia* spp. Supplementation Increases CAR T-cell Potency. Cancer Discov. *15*, 1905–1926. https://doi.org/10.1158/2159-8290.CD-24-1230.

19. Hubbard, T.D., Murray, I.A., Bisson, W.H., Lahoti, T.S., Gowda, K., Amin, S.G., Patterson, A.D., and Perdew, G.H. (2015). Adaptation of the human aryl hydrocarbon receptor to sense microbiota-derived indoles. Sci. Rep. *5*, 12689. https://doi.org/10.1038/srep12689.

20. Zelante, T., Iannitti, R.G., Cunha, C., De Luca, A., Giovannini, G., Pieraccini, G., Zecchi, R., D'Angelo, C., Massi-Benedetti, C., Fallarino, F., et al. (2013). Tryptophan Catabolites from Microbiota Engage Aryl Hydrocarbon Receptor and Balance Mucosal Reactivity via Interleukin-22. Immunity *39*, 372–385. https://doi.org/10.1016/j.immuni.2013.08.003.

21. Argüello, R.J., Combes, A.J., Char, R., Gigan, J.-P., Baaziz, A.I., Bousiquot, E., Camosseto, V., Samad, B., Tsui, J., Yan, P., et al. (2020). SCENITH: A Flow Cytometry-Based Method to Functionally Profile Energy Metabolism with Single-Cell Resolution. Cell Metab. *32*, 1063–1075.e7. https://doi.org/10.1016/j.cmet.2020.11.007.

22. Stein-Thoeringer, C.K., Nichols, K.B., Lazrak, A., Docampo, M.D., Slingerland, A.E., Slingerland, J.B., Clurman, A.G., Armijo, G., Gomes, A.L.C., Shono, Y., et al. (2019). Lactose drives *Enterococcus* expansion to promote graft-versus-host disease. Science *366*, 1143–1149. https://doi.org/10.1126/science.aax3760.

23. DeGruttola, A.K., Low, D., Mizoguchi, A., and Mizoguchi, E. (2016). Current Understanding of Dysbiosis in Disease in Human and Animal Models. Inflamm. Bowel Dis. *22*, 1137–1150. https://doi.org/10.1097/MIB.0000000000000750.

24. Rigottier-Gois, L. (2013). Dysbiosis in inflammatory bowel diseases: the oxygen hypothesis. ISME J. *7*, 1256–1261. https://doi.org/10.1038/ismej.2013.80.

25. Joos, R., Boucher, K., Lavelle, A., Arumugam, M., Blaser, M.J., Claesson, M.J., Clarke, G., Cotter, P.D., De Sordi, L., Dominguez-Bello, M.G., et al. (2025). Examining the healthy human microbiome concept. Nat. Rev. Microbiol. *23*, 192–205. https://doi.org/10.1038/s41579-024-01107-0.

26. Nicholson, J.K., Holmes, E., Kinross, J., Burcelin, R., Gibson, G., Jia, W., and Pettersson, S. (2012). Host-gut microbiota metabolic interactions. Science *336*, 1262–1267. https://doi.org/10.1126/science.1223813.

27. Zhang, J., Zhong, J., Cui, Z., Shen, Y., Zheng, Y., Zhang, Y., Man, C., Hou, Y., Zhao, Q., and Jiang, Y. (2024). Branched-chain fatty acids from goat milk alleviate ulcerative colitis *via* the TLR4/NF-κB/NLRP3 pathway. Food Sci. Hum. Wellness *13*, 3624–3632. https://doi.org/10.26599/FSHW.2023.9250044.

28. Yachida, S., Mizutani, S., Shiroma, H., Shiba, S., Nakajima, T., Sakamoto, T., Watanabe, H., Masuda, K., Nishimoto, Y., Kubo, M., et al. (2019). Metagenomic and metabolomic analyses reveal distinct stage-specific phenotypes of the gut microbiota in colorectal cancer. Nat. Med. *25*, 968–976. https://doi.org/10.1038/s41591-019-0458-7.

29. Chen, J., Su, R., He, Y., and Chen, J. (2025). Intermittent fasting inhibits the development of colorectal cancer in APC Min/+ mice through gut microbiota and its related metabolites. Front. Microbiol. *16*, 1563224. https://doi.org/10.3389/fmicb.2025.1563224.

30. Manna, S., Maiti, S., Shen, J., Weiss, A., Mulder, E., Du, W., and Esser-Kahn, A.P. (2023). Nanovaccine that activates the NLRP3 inflammasome enhances tumor specific activation of anti-cancer immunity. Biomaterials *296*, 122062. https://doi.org/10.1016/j.biomaterials.2023.122062.

31. Agus, A., Planchais, J., and Sokol, H. (2018). Gut Microbiota Regulation of Tryptophan Metabolism in Health and Disease. Cell Host Microbe *23*, 716–724. https://doi.org/10.1016/j.chom.2018.05.003.

32. Liu, Y., Liang, X., Yin, X., Lv, J., Tang, K., Ma, J., Ji, T., Zhang, H., Dong, W., Jin, X., et al. (2017). Blockade of IDO-kynurenine-AhR metabolic circuitry abrogates IFN-γ-induced immunologic dormancy of tumor-repopulating cells. Nat. Commun. *8*, 15207. https://doi.org/10.1038/ncomms15207.

33. Siska, P.J., Jiao, J., Matos, C., Singer, K., Berger, R.S., Dettmer, K., Oefner, P.J., Cully, M.D., Wang, Z., QuinnIII, W.J., III., et al. (2021). Kynurenine induces T cell fat catabolism and has limited suppressive effects in vivo. EBiomedicine *74*, 103734. https://doi.org/10.1016/j.ebiom.2021.103734.

34. Opitz, C.A., Litzenburger, U.M., Sahm, F., Ott, M., Tritschler, I., Trump, S., Schumacher, T., Jestaedt, L., Schrenk, D., Weller, M., et al. (2011). An endogenous tumour-promoting ligand of the human aryl hydrocarbon receptor. Nature *478*, 197–203. https://doi.org/10.1038/nature10491.

35. Frumento, G., Rotondo, R., Tonetti, M., Damonte, G., Benatti, U., and Ferrara, G.B. (2002). Tryptophan-derived Catabolites Are Responsible for Inhibition of T and Natural Killer Cell Proliferation Induced by Indoleamine 2,3-Dioxygenase. J. Exp. Med. *196*, 459–468. https://doi.org/10.1084/jem.20020121.

36. Chen, Y., Zhang, L., Zhang, L., Jiang, Q., and Zhang, L. (2021). Discovery of indole-3-butyric acid derivatives as potent histone deacetylase

inhibitors. J. Enzyme Inhib. Med. Chem. *36*, 425–436. https://doi.org/10.1080/14756366.2020.1870457.

37. Mimori, S., Kawada, K., Saito, R., Takahashi, M., Mizoi, K., Okuma, Y., Hosokawa, M., and Kanzaki, T. (2019). Indole-3-propionic acid has chemical chaperone activity and suppresses endoplasmic reticulum stress-induced neuronal cell death. Biochem. Biophys. Res. Commun. *517*, 623–628. https://doi.org/10.1016/j.bbrc.2019.07.074.
38. Jia, D., Wang, Q., Qi, Y., Jiang, Y., He, J., Lin, Y., Sun, Y., Xu, J., Chen, W., Fan, L., et al. (2024). Microbial metabolite enhances immunotherapy efficacy by modulating T cell stemness in pan-cancer. Cell *187*, 1651–1665.e21. https://doi.org/10.1016/j.cell.2024.02.022.
39. Bender, M.J., McPherson, A.C., Phelps, C.M., Pandey, S.P., Laughlin, C.R., Shapira, J.H., Medina Sanchez, L., Rana, M., Richie, T.G., Mims, T.S., et al. (2023). Dietary tryptophan metabolite released by intratumoral Lactobacillus reuteri facilitates immune checkpoint inhibitor treatment. Cell *186*, 1846–1862.e26. https://doi.org/10.1016/j.cell.2023.03.011.
40. Lawrence, B.P., Roberts, A.D., Neumiller, J.J., Cundiff, J.A., and Woodland, D.L. (2006). Aryl Hydrocarbon Receptor Activation Impairs the Priming but Not the Recall of Influenza Virus-Specific CD8+ T Cells in the Lung. J. Immunol. *177*, 5819–5828. https://doi.org/10.4049/jimmunol.177.9.5819.
41. Winans, B., Nagari, A., Chae, M., Post, C.M., Ko, C.-I., Puga, A., Kraus, W.L., and Lawrence, B.P. (2015). Linking the Aryl Hydrocarbon Receptor with Altered DNA Methylation Patterns and Developmentally Induced Aberrant Antiviral CD8+ T Cell Responses. J. Immunol. *194*, 4446–4457. https://doi.org/10.4049/jimmunol.1402044.
42. Gutiérrez-Vázquez, C., and Quintana, F.J. (2018). Regulation of the Immune Response by the Aryl Hydrocarbon Receptor. Immunity *48*, 19–33. https://doi.org/10.1016/j.immuni.2017.12.012.
43. Dean, J.W., Helm, E.Y., Fu, Z., Xiong, L., Sun, N., Oliff, K.N., Muehlbauer, M., Avram, D., and Zhou, L. (2023). The aryl hydrocarbon receptor cell intrinsically promotes resident memory CD8+ T cell differentiation and function. Cell Rep. *42*, 111963. https://doi.org/10.1016/j.celrep.2022.111963.
44. Ma, M.-Y., Hu, L.-L., Xu, W.-Y., and Zhang, W. (2024). L-tryptophan anaerobic fermentation for indole acetic acid production: Bacterial enrichment and effects of zero valent iron. Bioresour. Technol. *400*, 130691. https://doi.org/10.1016/j.biortech.2024.130691.
45. Perl, M., Fante, M.A., Herfeld, K., Scherer, J.N., Poeck, H., and Thiele Orberg, E. (2025). Microbiota-derived metabolites: Key modulators of cancer immunotherapies. Med. *6*, 100773. https://doi.org/10.1016/j.medj.2025.100773.
46. Santos, E.B., Yeh, R., Lee, J., Nikhamin, Y., Punzalan, B., Punzalan, B., La Perle, K.L., Larson, S.M., Sadelain, M., and Brentjens, R.J. (2009). Sensitive in vivo imaging of T cells using a membrane-bound Gaussia princeps luciferase. Nat. Med. *15*, 338–344. https://doi.org/10.1038/nm.1930.
47. Chewning, J.H., Dugger, K.J., Chaudhuri, T.R., Zinn, K.R., and Weaver, C.T. (2009). Bioluminescence-based visualization of CD4 T cell dynamics using a T lineage-specific luciferase transgenic model. BMC Immunol. *10*, 44. https://doi.org/10.1186/1471-2172-10-44.
48. Rodriguez, J., Hassani, Z., Alves Costa Silva, C., Betsou, F., Carraturo, F., Fasano, A., Israelsen, M., Iyappan, A., Krag, A., Metwaly, A., et al. (2025). State of the art and the future of microbiome-based biomarkers: a multidisciplinary Delphi consensus. Lancet Microbe *6*, 100948. https://doi.org/10.1016/j.lanmic.2024.07.011.
49. Jankovic, D., Ganesan, J., Bscheider, M., Stickel, N., Weber, F.C., Guarda, G., Follo, M., Pfeifer, D., Tardivel, A., Ludigs, K., et al. (2013). The Nlrp3 inflammasome regulates acute graft-versus-host disease. J. Exp. Med. *210*, 1899–1910. https://doi.org/10.1084/jem.20130084.
50. Sabatino, M., Hu, J., Sommariva, M., Gautam, S., Fellowes, V., Hocker, J.D., Dougherty, S., Qin, H., Klebanoff, C.A., Fry, T.J., et al. (2016). Generation of clinical-grade CD19-specific CAR-modified CD8+ memory stem cells for the treatment of human B-cell malignancies. Blood *128*, 519–528. https://doi.org/10.1182/blood-2015-11-683847.
51. Kochenderfer, J.N., Feldman, S.A., Zhao, Y., Xu, H., Black, M.A., Morgan, R.A., Wilson, W.H., and Rosenberg, S.A. (2009). Construction and Preclinical Evaluation of an Anti-CD19 Chimeric Antigen Receptor. J. Immunother. *32*, 689–702. https://doi.org/10.1097/CJI.0b013e3181ac6138.
52. Wu, T., Hu, E., Xu, S., Chen, M., Guo, P., Dai, Z., Feng, T., Zhou, L., Tang, W., Zhan, L., et al. (2021). clusterProfiler 4.0: A universal enrichment tool for interpreting omics data. Innovation (Camb.) *2*, 100141. https://doi.org/10.1016/j.xinn.2021.100141.
53. Friedman, J., Hastie, T., and Tibshirani, R. (2010). Regularization Paths for Generalized Linear Models via Coordinate Descent. J. Stat. Softw. *33*, 1–22. https://doi.org/10.18637/jss.v033.i01.
54. Korsunsky, I., Millard, N., Fan, J., Slowikowski, K., Zhang, F., Wei, K., Baglaenko, Y., Brenner, M., Loh, P.-R., and Raychaudhuri, S. (2019). Fast, sensitive and accurate integration of single-cell data with Harmony. Nat. Methods *16*, 1289–1296. https://doi.org/10.1038/s41592-019-0619-0.
55. Beghini, F., McIver, L.J., Blanco-Míguez, A., Dubois, L., Asnicar, F., Maharjan, S., Mailyan, A., Manghi, P., Scholz, M., Thomas, A.M., et al. (2021). Integrating taxonomic, functional, and strain-level profiling of diverse microbial communities with bioBakery 3. eLife *10*, e65088. https://doi.org/10.7554/eLife.65088.
56. Khleborodova, A., Gamboa-Tuz, S.D., Ramos, M., Segata, N., Waldron, L., and Oh, S. (2024). lefser: implementation of metagenomic biomarker discovery tool, LEfSe, in R. Bioinformatics *40*, btae707. https://doi.org/10.1093/bioinformatics/btae707.
57. Segata, N., Izard, J., Waldron, L., Gevers, D., Miropolsky, L., Garrett, W.S., and Huttenhower, C. (2011). Metagenomic biomarker discovery and explanation. Genome Biol. *12*, R60. https://doi.org/10.1186/gb-2011-12-6-r60.
58. Nickols, W.A., Kuntz, T., Shen, J., Maharjan, S., Mallick, H., Franzosa, E.A., Thompson, K.N., Nearing, J.T., and Huttenhower, C. (2026). MaAsLin 3: refining and extending generalized multivariable linear models for meta-omic association discovery. Nat. Methods *23*, 554–564. https://doi.org/10.1038/s41592-025-02923-9.
59. Blanco-Míguez, A., Beghini, F., Cumbo, F., McIver, L.J., Thompson, K.N., Zolfo, M., Manghi, P., Dubois, L., Huang, K.D., Thomas, A.M., et al. (2023). Extending and improving metagenomic taxonomic profiling with uncharacterized species using MetaPhlAn 4. Nat. Biotechnol. *41*, 1633–1644. https://doi.org/10.1038/s41587-023-01688-w.
60. Zhou, H., He, K., Chen, J., and Zhang, X. (2022). LinDA: linear models for differential abundance analysis of microbiome compositional data. Genome Biol. *23*, 95. https://doi.org/10.1186/s13059-022-02655-5.
61. Subramanian, A., Tamayo, P., Mootha, V.K., Mukherjee, S., Ebert, B.L., Gillette, M.A., Paulovich, A., Pomeroy, S.L., Golub, T.R., Lander, E.S., et al. (2005). Gene set enrichment analysis: a knowledge-based approach for interpreting genome-wide expression profiles. Proc. Natl. Acad. Sci. USA *102*, 15545–15550. https://doi.org/10.1073/pnas.0506580102.
62. Liberzon, A., Birger, C., Thorvaldsdóttir, H., Ghandi, M., Mesirov, J.P., and Tamayo, P. (2015). The Molecular Signatures Database (MSigDB) hallmark gene set collection. Cell Syst. *1*, 417–425. https://doi.org/10.1016/j.cels.2015.12.004.
63. He, L., Davila-Velderrain, J., Sumida, T.S., Hafler, D.A., Kellis, M., and Kulminski, A.M. (2021). NEBULA is a fast negative binomial mixed model for differential or co-expression analysis of large-scale multi-subject single-cell data. Commun. Biol. *4*, 629. https://doi.org/10.1038/s42003-021-02146-6.
64. McMurdie, P.J., and Holmes, S. (2013). phyloseq: an R package for reproducible interactive analysis and graphics of microbiome census data. PLoS One *8*, e61217. https://doi.org/10.1371/journal.pone.0061217.
65. Sayols, S. (2023). rrvgo: a Bioconductor package for interpreting lists of Gene Ontology terms. MicroPubl Biol. *2023*. https://doi.org/10.17912/micropub.biology.000811.
66. Germain, P.-L., Lun, A., Garcia Meixide, C., Macnair, W., and Robinson, M.D. (2021). Doublet identification in single-cell sequencing data using

scDblFinder. F1000Res *10*, 979. https://doi.org/10.12688/f1000research.73600.2.

67. Hao, Y., Hao, S., Andersen-Nissen, E., Mauck, W.M., Zheng, S., Butler, A., Lee, M.J., Wilk, A.J., Darby, C., Zager, M., et al. (2021). Integrated analysis of multimodal single-cell data. Cell *184*, 3573–3587.e29. https://doi.org/10.1016/j.cell.2021.04.048.
68. Bhardwaj, V., Heyne, S., Sikora, K., Rabbani, L., Rauer, M., Kilpert, F., Richter, A.S., Ryan, D.P., and Manke, T. (2019). snakePipes: facilitating flexible, scalable and integrative epigenomic analysis. Bioinformatics *35*, 4757–4759. https://doi.org/10.1093/bioinformatics/btz436.
69. Dobin, A., Davis, C.A., Schlesinger, F., Drenkow, J., Zaleski, C., Jha, S., Batut, P., Chaisson, M., and Gingeras, T.R. (2013). STAR: ultrafast universal RNA-seq aligner. Bioinformatics *29*, 15–21. https://doi.org/10.1093/bioinformatics/bts635.
70. Liao, Y., Smyth, G.K., and Shi, W. (2014). featureCounts: an efficient general purpose program for assigning sequence reads to genomic features. Bioinformatics *30*, 923–930. https://doi.org/10.1093/bioinformatics/btt656.
71. Wickham, H., Averick, M., Bryan, J., Chang, W., McGowan, L., François, R., Grolemund, G., Hayes, A., Henry, L., Hester, J., et al. (2019). Welcome to the Tidyverse. JOSS *4*, 1686. https://doi.org/10.21105/joss.01686.
72. Martin, M. (2011). Cutadapt removes adapter sequences from high-throughput sequencing reads. EMBnet J. *17*, 10. https://doi.org/10.14806/ej.17.1.200.
73. Thiele Orberg, E., Meedt, E., Hiergeist, A., Xue, J., Heinrich, P., Ru, J., Ghimire, S., Miltiadous, O., Lindner, S., Tiefgraber, M., et al. (2024). Bacteria and Bacteriophage Consortia Are Associated with Protective Intestinal Metabolites in Patients Receiving Stem Cell Transplantation. Nat. Cancer *5*, 187–208. https://doi.org/10.1038/s43018-023-00669-x.
74. Hernandez-Lopez, R.A., Yu, W., Cabral, K.A., Creasey, O.A., Lopez Pazmino, M.D.P., Tonai, Y., De Guzman, A., Mäkelä, A., Saksela, K., Gartner, Z.J., et al. (2021). T cell circuits that sense antigen density with an ultrasensitive threshold. Science *371*, 1166–1171. https://doi.org/10.1126/science.abc1855.
75. Kochenderfer, J.N., Yu, Z., Frasheri, D., Restifo, N.P., and Rosenberg, S.A. (2010). Adoptive transfer of syngeneic T cells transduced with a chimeric antigen receptor that recognizes murine CD19 can eradicate lymphoma and normal B cells. Blood *116*, 3875–3886. https://doi.org/10.1182/blood-2010-01-265041.
76. Luu, M., Pautz, S., Kohl, V., Singh, R., Romero, R., Lucas, S., Hofmann, J., Raifer, H., Vachharajani, N., Carrascosa, L.C., et al. (2019). The short-chain fatty acid pentanoate suppresses autoimmunity by modulating the metabolic-epigenetic crosstalk in lymphocytes. Nat. Commun. *10*, 760. https://doi.org/10.1038/s41467-019-08711-2.
77. Göttert, S., Thiele Orberg, E., Fan, K., Heinrich, P., Matthe, D.M., Khalid, O., Klostermeier, L., Suriano, C., Strieder, N., Gebhard, C., et al. (2025). The microbial metabolite desaminotyrosine protects against graft-versus-host disease via mTORC1 and STING-dependent intestinal regeneration. Nat. Commun. *16*, 9282. https://doi.org/10.1038/s41467-025-65180-6.
78. Tintelnot, J., Xu, Y., Lesker, T.R., Schönlein, M., Konczalla, L., Giannou, A.D., Pelczar, P., Kylies, D., Puelles, V.G., Bielecka, A.A., et al. (2023). Microbiota-derived 3-IAA influences chemotherapy efficacy in pancreatic cancer. Nature *615*, 168–174. https://doi.org/10.1038/s41586-023-05728-y.
79. Hao, Y., Stuart, T., Kowalski, M.H., Choudhary, S., Hoffman, P., Hartman, A., Srivastava, A., Molla, G., Madad, S., Fernandez-Granda, C., et al. (2024). Dictionary learning for integrative, multimodal and scalable single-cell analysis. Nat. Biotechnol. *42*, 293–304. https://doi.org/10.1038/s41587-023-01767-y.
80. Andreatta, M., and Carmona, S.J. (2021). UCell: Robust and scalable single-cell gene signature scoring. Comput. Struct. Biotechnol. J. *19*, 3796–3798. https://doi.org/10.1016/j.csbj.2021.06.043.
81. Tirosh, I., Izar, B., Prakadan, S.M., Wadsworth, M.H., Treacy, D., Trombetta, J.J., Rotem, A., Rodman, C., Lian, C., Murphy, G., et al. (2016). Dissecting the multicellular ecosystem of metastatic melanoma by single-cell RNA-seq. Science *352*, 189–196. https://doi.org/10.1126/science.aad0501.
82. McInnes, L., Healy, J., Saul, N., and Großberger, L. (2018). UMAP: Uniform Manifold Approximation and Projection. JOSS *3*, 861. https://doi.org/10.21105/joss.00861.
83. Venables, W.N., and Ripley, B.D. (2002). Modern Applied Statistics with S (Springer). https://doi.org/10.1007/978-0-387-21706-2.

STAR★METHODS

KEY RESOURCES TABLE

REAGENT or RESOURCE	SOURCE	IDENTIFIER
Antibodies		
Acetyl-CoA Carboxylase (C83B10) Rabbit mAb	Cell Signaling	Cat# 3676; RRID:AB_2219397
Acetyl-CoA Carboxylase (C83B10) Rabbit mAb	Cell Signaling	Cat# 3676; RRID:AB_2219397
AF647 anti-rat CD90/mouse CD90.1 (Thy-1.1)	Biolegend	Cat# 202508; RRID:AB_492884
AF647, anti-Puromycin (12D10), 12D10	Merck	Cat# MABE343-AF647; RRID:AB_2736876
Anti-mouse IgG, HRP-linked Antibody	Cell Signaling	Cat# 7076; RRID:AB_330924
Anti-rabbit IgG, HRP-linked Antibody	Cell Siganling	Cat# 7074; RRID:AB_2099233
APC anti-mouse CD8a	Biolegend	Cat# 100712; RRID:AB_31275
APC, anti-human IFN-γ 4S.B3	Biolegend	Cat# 502512; RRID:AB_315237
BB700 Rat Anti-Mouse CD19, 0.1 mg	BD Biosciences	Cat# 566411; RRID:AB_2744315
BB700, anti-mouse CD19, 1D3	BD Biosciences	Cat# 566411; RRID:AB_2744315
Biotin, anti-human c-myc, SH1-26 E7.1.3	Miltenyi Biotec	Cat# 130-124-877; RRID:AB_2889650
Brilliant Violet 421™, anti-human CD279 (PD-1), NAT105	Biolegend	Cat# 367422; RRID:AB_2721517
Brilliant Violet 785™, anti-human CD3, OKT3	Biolegend	Cat# 317330; RRID:AB_2563507
BUV395, anti-mouse CD3, 17A2	Thermo Fisher Scientific	Cat# 363-0032-82; RRID:AB_2937086
BUV737 Mouse Anti-Human CD25	BD Biosciences	Cat# 612806; RRID:AB_2870132
BUV805 anti-rat CD90/mouse CD90.1, OX-7	BD Biosciences	Cat# 741975; RRID:AB_2871279
BUV805, anti-human CD8, HIT8a	BD Biosciences	Cat# 742030; RRID:AB_2871326
BV421 anti-mouse CD274 (B7-H1, PD-L1)	Biolegend	Cat# 124315; RRID:AB_10897097
BV421, anti-human CD3, UCHT1	Biolegend	Cat# 300434; RRID:AB_10962690
BV605, anti-human TIM-3 (CD366), 7D3	BD Biosciences	Cat# 569245; RRID:AB_2741099
BV650, anti-human T-bet, O4-46	BD Biosciences	Cat# 564142; RRID:AB_2738616
BV711 anti-mouse CD19	Biolegend	Cat# 115555; RRID:AB_2565970
BV711, anti-human CD4, SK3	BD Biosciences	Cat# 563028; RRID:AB_2737961
FITC anti-mouse CD3, 500 μg	Biolegend	Cat# 100204; RRID:AB_312661
FITC, anti-human c-myc, SH1-26E7.1.3	Miltenyi Biotec	Cat# 130-116-485; RRID:AB_2751329

(*Continued on next page*)

Continued

REAGENT or RESOURCE	SOURCE	IDENTIFIER
FITC, anti-human FMC63 scFv, Y45	Acro Biosystems	Cat# FM3-FY45-25tests; RRID:AB_2921284
Histone H3 (D1H2) XP Rabbit mAb	Cell Signaling	Cat# 4499; RRID:AB_10544537
mTOR (7C10) Rabbit mAb	Cell Signaling	Cat# 2983; RRID:AB_2105622
Myc-Tag (71D10) Rabbit Monoclonal Antibody (AF 488 Conjug.)	Cell Siganling	Cat# 40760; RRID:AB_1658203
PB anti mouse CD4, 0.1 mg	BD Biosciences	Cat# 558107; RRID:AB_2739450
PE anti MCL-1, LVUBKM	Thermo	Cat# 12-9047-42; RRID:AB_2762598
PE anti-rat CD90/mouse CD90.1 (Thy-1.1)	Biolegend	Cat# 202524; RRID:AB_1107694
PE-Cy7, EOMES (WD1928)	Thermo Fisher Scientific	Cat# 25-4877-42; RRID:AB_2573456
PE-Cyanine7, anti-human Eomes, WD1928	Thermo Fisher Scientific	Cat# 25-4877-42; RRID:AB_2573456
PE, Streptavidin	Biolegend	Cat# 405204
PE/Cy7 anti-human CD8, 100 tests	Biolegend	Cat# 344712; RRID:AB_2044008
PE/Dazzle™ 594, anti-human/mouse Granzyme B, QA16A02	Biolegend	Cat# 372216; RRID:AB_2728382
PerCP-Cy5.5 anti-CD8, 0.1 mg	BD Biosciences	Cat# 551162; RRID:AB_394081
Phospho-Acetyl-CoA Carboxylase (Ser79) (D7D11) Rabbit Antibody	Cell Signaling	Cat# 11818; RRID:AB_2687505
Phospho-mTOR (Ser2448) (D9C2) XP Rabbit mAb	Cell Signaling	Cat# 5536; RRID:AB_10691552
Phospho-Pyruvate Dehydrogenase α1 (Ser293) (E4V9L) Rabbit mAb	Cell Signaling	Cat# 37115; RRID:AB_2923272
Phospho-S6 Ribosomal Protein (Ser235/236) (D57.2.2E) XP Rabbit mAb	Cell Signaling	Cat# 4858; RRID:AB_916156
Rabbit Anti-Histone H3, acetyl (Lys9) Monoclonal Antibody, Unconjugated, Clone C5B11	Cell Signaling	Cat# 9649; RRID:AB_823528
Rabbit Anti-Pyruvate Dehydrogenase Monoclonal Antibody, Unconjugated, Clone C54G1	Cell Signaling	Cat# 3205; RRID:AB_2162926
Rabbit Anti-S6 Ribosomal Protein Monoclonal Antibody, Unconjugated, Clone 5G10	Cell Signaling	Cat# 2217; RRID:AB_331355
β-Actin (8H10D10) Mouse mAb	Cell Signaling	Cat# 3700; RRID:AB_2242334
Biological samples		
Human peripheral blood mononuclear cells from healthy donors	This paper	N/A
Mouse Splenocytes	This paper	N/A
Chemicals, peptides, and recombinant proteins		
10x Tris/Glycine/SDS, 1l	Bio-Rad Laboratories, Inc	1610732
2-deoxy-D-glucose (2-DG; 100 mM)	Sigma-Aldrich	D6134-5G
2-mercaptoethanol	Bio-Rad Laboratories, Inc	1610710
4x Laemmli Sample Buffer, 10 ml	Bio-Rad Laboratories, Inc	1610747
Albumin, Bovine (BSA), IgG free	Roth	3737.3
CellTrace™ CFSE	Thermo Fisher Scientific	C34554

(*Continued on next page*)

Continued

REAGENT or RESOURCE	SOURCE	IDENTIFIER
DMEM-high glucose	Sigma-Aldrich	D6429
DMSO	Roth	A994.1
EveryBlot Blocking Buffer, 500 ml	Bio-Rad Laboratories, Inc	12010020
FBS	PAN Biotech	P40-37500
Gelatine solution 0.1 % in DPBS	Pan Biotech	P06-20410
GlutaMax	Thermo Fisher Scientific	35050061
Harringtonine (2 μg/mL)	Santa Cruz Biotechnology	sc-204771
HEPES	Thermo Fisher Scientific	15630-056
Human recombinant IL-15	Miltenyi Biotec	130-095-765
Human recombinant IL-2	Miltenyi Biotec	130-097-745
Human recombinant IL-7	Miltenyi Biotec	130-095-362
Indole-3-acetic acid (IAA)	Sigma-Aldrich	13750-25G-A
Indole-3-carboxaldehyde (ICA)	Sigma-Aldrich	129445-25G
Isoflurane	Piramal Critical Care	9714675
Isovaleric acid	Sigma-Aldrich	129542
IVISbrite™ D-Luciferin	Revvity	122799–5
L-glutamine	Thermo Fisher Scientific	25030024
MEM non-essential amino acid solution	Sigma-Aldrich	M7145
MEM Vitamin Solution (100×)	Sigma-Aldrich	M6895
OptiMEM	Thermo Fisher Scientific	31985062
Pancoll™ Cell Separation Medium	PAN Biotech	P04-601000
PEG 400	Sigma-Aldrich	8.07485
Penicillin-streptomycin	Thermo Fisher Scientific	15140–122
Polybrene	Sigma-Aldrich	TR-1003
Puromycin (10 μg/mL)	Sigma-Aldrich	P7255-25mg
Q5 high fidelity polymerase	New England Biolabs	M0491S
Recombinant human CD19 protein (ECD, His & AVI Tag)	Sino Biological	11880-H49H-B
Recombinant human HER2/ERBB2 protein (ECD, hFc-tag)	Sino Biological	10004-H02H
RetroNectin	Takara Bio	T100B
RPMI 1640	PAN Biotech	31870-074
Sodium pyruvate	Thermo Fisher Scientific	11360070
Sterile H20	Invitrogen™	Thermo Fisher Scientific
Trypsin-EDTA (0,05 %), phenol red	Thermo Fisher Scientific	25300062
Valeric acid (pentanoate)	Sigma-Aldrich	W310107-1KG-K
Critical commercial assays		
Cytofix/Cytoperm™ Fixation/ Permeabilization Kit	BD Biosciences	554714
eBioscience™ Foxp3 / Transcription Factor Staining Buffer Set	Invitrogen	00-5523-00
HDAC2 fluorogenic kit	Biomol	BPS-50062
High Sensitivity RNA ScreenTape Ladder	Agilent	5067–5581
High Sensitivity RNA ScreenTape Sample Buffer	Agilent	5067–5580
High Sensitivity RNA ScreenTape	Agilent	5067–5579
Lipofectamine 3000 Kit	Thermo Fisher Scientific	L3000015
Lonza™ P3 Primary Cell 4D-Nucleofector™ X Kit L	Lonza	V4XP-3012

(*Continued on next page*)

Continued

REAGENT or RESOURCE	SOURCE	IDENTIFIER
Lonza™ P3 Primary Cell 4D-Nucleofector™ X Kit S	Lonza	V4XP-3032
Maxwell® RSC Fecal Microbiome DNA Kit	Promega	AS1700
Pan T Cell Isolation Kit, human	Miltenyi Biotec	130-096-535
Pure Link HiPure Plasmid Midiprep Kit	Thermo Fisher Scientific	K210004
TrueCut™ Cas9 Protein v2	Thermo Fisher Scientific	A36498
Trans-Blot Turbo Mini 0.2 µm PVDF Transfer Packs	Bio-Rad Laboratories, Inc	1704156
12% Mini-PROTEAN Protein Gels, 12 wells, 20 µl, pkg of 10	Bio-Rad Laboratories, Inc	4568045
GEM-X Universal 3′ Gene Expression v4 4-plex (OCM), 16 samples	10X Genomics	1000779
GEM-X OCM 3′ Chip Kit v4 4-plex, 2 chips	10X Genomics	1000747
Quant Seq 3′mRNA V2 library prep kit FWD with UDI 12ntSet B1 (96 samples)	Lexogen	192.96
Rneasy Mini Kit	Qiagen	74104
XLEAP-SBS NextSeq 1000/2000 P^2 100 Cycle	Illumina	20100987
XLEAP-SBS NextSeq 1000/2000 P4 100 Cycle	Illumina	20100994
Deposited data		
CAR T patient metagenomic sequencing data	This paper	ENA: PRJEB101146
CAR T patient targeted mass spectrometry data	This paper	MassIVE: MSV000101883 https://doi.org/10.5281/zenodo.17475484
CAR T scRNA-seq data	This paper	EGA: EGAS50000001386
Metabolite treated A20 bulk RNA-Seq data	This paper	GEO: GSE329624
Mouse gavage targeted mass spectrometry data	This paper	MassIVE: MSV000101884 https://doi.org/10.5281/zenodo.20085233
Experimental models: Cell lines		
A20/Luc cells	Jankovic et al.[49]	N/A
HEK293T	ATCC	RRID:CVCL_0063
NALM-6 GFP/Luc	Sabatino et al.[50]	N/A
PG13 producer cell line	Kochenderfer et al.[51]	N/A
Phoenix Eco	ATCC	RRID:CVCL_H717
SKOV3	ATCC	RRID:CVCL_0532
Experimental models: Organisms/strains		
NXG mice (NOD-*Prkdc*^{scid}-*IL2rg*^{Tm1}/Rj, female)	Janvier Labs	N/A
BALB/cJRj (female)	Janvier Labs	N/A
Oligonucleotides		
Alt-R® CRISPR-Cas9 tracrRNA	IDT	1072534
AHR_forward primer (GGAATCACTGTGCTACAAATGC)	Sigma-Aldrich	N/A
AHR_reverse primer (TTCAGTGGCTGCATCTGTTG)	Sigma-Aldrich	N/A
crRNA AHR_1 (TCAAGTCAAATCCTTCCAAG)	IDT	Hs.Cas9.AHR.1.AX
crRNA AHR_2 (CATCTTGTGGGAAAGGCAC)	IDT	AHR_gRNA_2

(*Continued on next page*)

Continued

REAGENT or RESOURCE	SOURCE	IDENTIFIER
Recombinant DNA		
pCL-Eco	Addgene	12371
pHR_SFFv_4D5-Low-CAR_RHL001 (Her2 CAR)	Addgene	164824
pMD2.G	Addgene	12259
pMSCV_1D3_CD28z_CD90.1 (encoding a murine anti-CD19 CAR	Vectorbuilder	N/A
psPAX2	Addgene	12260
Software and algorithms		
AnnotationDbi v1.72.0	N/A	https://bioconductor.org/packages/AnnotationDbi/ RRID:SCR_023487
bcl2convert v3.8.4	Illumina	https://support.illumina.com/downloads/bcl-convert-v4-4-6-installers.html
Benchling	Benchling	https://www.benchling.com/ RRID:SCR_013955
Biorender	BioRender	https://www.biorender.com/
BulkRNA-Seq analysis code	This Work	https://github.com/lit-regensburg/IMM-CART-Paper_RNASeq-A20
Cell Ranger v9.0.1	10x Genomics	https://www.10xgenomics.com/support/software/cell-ranger/latest RRID:SCR_017344
clusterProfiler v4.18.4	Wu et al.[52]	https://bioconductor.org/packages/clusterProfiler/ RRID:SCR_016884
DEGreport v1.46.0	N/A	https://bioconductor.org/packages/DEGreport/ RRID:SCR_018941
DescTools v0.99.60	N/A	https://cran.r-project.org/package=DescTools,RRID:SCR_027454
DESeq2 v1.50.2	N/A	https://bioconductor.org/packages/DESeq2/ RRID:SCR_015687
enrichplot v1.30.5	N/A	https://bioconductor.org/packages/enrichplot/ RRID:SCR_026996
fgsea v1.26.0	N/A	https://bioconductor.org/packages/fgsea/ RRID:SCR_020938
FlowJo software 10.9.0	Tree Star	https://www.flowjo.com/
ggbeeswarm v0.7.2	N/A	https://cran.r-project.org/package=ggbeeswarm RRID:SCR_026875
ggprism v1.0.6	N/A	https://cran.r-project.org/package=ggprism
ggpubr v0.6.0	N/A	https://cran.r-project.org/package=ggpubr RRID:SCR_021139
glmnet v4.1-8	Friedman et al.[53]	https://cran.r-project.org/package=glmnet RRID:SCR_015505
Harmony v1.2.0	Korsunsky et al.[54]	https://cran.r-project.org/package=harmony RRID:SCR_022206
HUMAnN v3	Beghini et al.[55]	https://github.com/biobakery/humann RRID:SCR_014620
Image Lab Touch v2.4.0.03	Bio-Rad Laboratories, Inc	RRID:SCR_014210
Image Lab v6.1.0 build 7	Bio-Rad Laboratories, Inc	RRID:SCR_014210

(*Continued on next page*)

Continued

REAGENT or RESOURCE	SOURCE	IDENTIFIER
Incucyte software v2024A	Sartorius	https://www.sartorius.com/en
Kneaddata	N/A	https://github.com/biobakery/kneaddata
lefser v1.16.2	Khleborodova et al.[56] and Segata et al.[57]	https://bioconductor.org/packages/lefser/
MaAsLin3 v0.99.16	Nickols et al.[58]	https://bioconductor.org/packages/maaslin3/
MASS v7.3.60	N/A	https://cran.r-project.org/package=MASS RRID:SCR_019125
MetaboAnalyst	Wishart Research Group, University of Alberta	https://www.metaboanalyst.ca/ RRID:SCR_015539
Metagenomics and Metabolomics analysis code	This Work	https://github.com/lit-regensburg/IMM-CART-Paper_MGX-MBX
MetaPhlAn v4.1.1	Blanco-Míguez et al.[59]	https://github.com/biobakery/metaphlan RRID:SCR_004915
microbiome v1.28.0	N/A	https://bioconductor.org/packages/microbiome/ RRID:SCR_024699
MicrobiomeStat v1.4.1	Zhou et al.[60]	https://cran.R-project.org/package=MicrobiomeStat
MSigDB v7.5.1	Subramanian et al.[61] and Liberzon et al.[62]	RRID:SCR_016863
MultiQuant v3.0.3, Sciex	Sciex	https://sciex.com/products/software/multiquant-software
NEBULA v1.5.3	He et al.[63]	https://cran.r-project.org/package=nebula
org.Mm.eg.db v3.22.0	N/A	https://bioconductor.org/packages/org.Mm.eg.db/ RRID:SCR_023488
patchwork v1.3.0	N/A	https://cran.r-project.org/package=patchwork RRID:SCR_024826
pheatmap v1.0.12	N/A	https://cran.R-project.org/package=pheatmap RRID:SCR_016418
phyloseq v1.50.0	McMurdie and Holmes[64]	https://bioconductor.org/packages/phyloseq/ RRID:SCR_013080
precrec v0.14.5	N/A	https://cran.r-project.org/package=precrec RRID:SCR_018659
Prism software v10	GraphPad Software	https://www.graphpad.com/features
pROC v1.18.5	N/A	https://cran.R-project.org/package=pROC RRID:SCR_024286
Python v3.9.7	N/A	RRID:SCR_024202
R v4.4.2	R Core Team	https://www.R-project.org/ RRID:SCR_001905
rrvgo v1.22.0	Sayols et al.[65]	https://bioconductor.org/packages/rrvgo/ RRID:SCR_026680
rstatix v0.7.2	N/A	https://cran.r-project.org/package=rstatix RRID:SCR_021240
scDblFinder v1.14.0	Germain et al.[66]	https://bioconductor.org/packages/scDblFinder/ RRID:SCR_022700
scRNA-Seq analysis code	This work	https://github.com/lit-regensburg/scRNA_CAR_T_metabolites
Seurat v5.0.1	Hao et al.[67]	https://cran.r-project.org/package=seurat RRID:SCR_007322
SingleCellExperiment v1.22.0	N/A	https://bioconductor.org/packages/SingleCellExperiment/ RRID:SCR_026794

(*Continued on next page*)

Continued

REAGENT or RESOURCE	SOURCE	IDENTIFIER
Snakemake v5.18.0	N/A	https://github.com/snakemake/snakemake RRID:SCR_003475
snakepipes v2.5.1	Bhardwaj et al.[68]	https://github.com/maxplanck-ie/snakepipes
STAR v2.7.4	Dobin et al.[69]	https://github.com/alexdobin/STAR RRID:SCR_004463
subread v2.0.0	Liao et al.[70]	https://github.com/ShiLab-Bioinformatics/subread RRID:SCR_009803
survival v3.8-3	N/A	https://cran.r-project.org/package=survival RRID:SCR_021137
survminer v0.5.0	N/A	https://cran.r-project.org/package=survminer RRID:SCR_021094
sva v3.54.0	N/A	https://bioconductor.org/packages/sva/ RRID:SCR_002155
tidyverse v2.0.0	Wickham et al.[71]	https://cran.r-project.org/package=tidyverse RRID:SCR_019186
Trim Galore v0.6.5	Babraham Institute[72]	https://github.com/felixkrueger/trimgalore RRID:SCR_011847
UMI-tools v1.0.1	N/A	https://github.com/CGATOxford/UMI-tools RRID:SCR_017048
vegan v2.6-10	N/A	https://cran.r-project.org/package=vegan RRID:SCR_011950
Other		
Brilliant Stain Buffer	BD Biosciences	566349
Cell Stimulation Cocktail plus protein transport inhibitor	Thermo Fisher Scientific	00-4975-03
Fixable Viability Dye eFluor 780	Thermo Fisher Scientific	65-0865-18
iNtRON G-DEX™ IIb RBC Lysis Buffer	HSS Diagnostics	172-R-1000
PageRuler Plus Prestained Protein Ladder, 2x250 µl	Thermo Fisher Scientific	26619
SuperSignal West Femto Maximum Sensitivity Substrat, 100 ml	Thermo Fisher Scientific	34095
T Cell TransAct™	Miltenyi Biotec	130-111-160
TransIT-293	Mirius Bio	MIR 5404
Treg Expansion Kit, mouse	Miltenyi Biotec	130-095-925
Ultracomp eBeads™ Plus	Invitrogen	01-3333-42
ReBlot Plus Mild Antibody Stripping Solution, 10x	Merck	2502
Zombie NIR Fixable Viability Kit	Biolegend	423105
Zombie UV Fixable Viability Kit	Biolegend	423108

EXPERIMENTAL MODEL AND STUDY PARTICIPANT DETAILS

Human Participants

The study cohort included 56 female and 73 male patients with a mean age of 61.5 years (range, 29–82 years). Sex was assigned based on electronic patient records. Male and female participants were comparably distributed across participating centersAs biological sex and self-reported gender identity were concordant for all participants, only biological sex was retained in the final dataset.

Age and sex were included as covariates in multivariable Cox proportional hazards regression models to assess their potential association with progression-free survival (PFS) and overall survival (OS).

Inclusion criteria were not based on race, ethnicity, or other socially constructed groupings; therefore, these variables were not specifically assessed in this study.

Peripheral blood mononuclear cells from healthy voluntary male and female donors aged 18–40 years were obtained from the Department of Transfusion Medicine, University Hospital Regensburg after informed consent. Donor sex was not considered during

sample selection and was not recorded in the study dataset. Gender identity was not available. Accordingly, potential effects of donor sex or gender were not assessed.

All procedures involving human participants were conducted in accordance with the Declaration of Helsinki and were approved by the local ethics committees of Regensburg (approval number 21-2521-101), Munich (approval number 19–817), and Heidelberg (#S-877/2019).

Cell lines

HEK293T (RRID:CVCL_0063) and Phoenix Eco (RRID:CVCL_H717) cells were obtained from ATCC. SKOV3 cells (RRID:CVCL_0532; ATCC) were engineered to express an EF1A-driven GFP/firefly luciferase construct. NALM-6 GFP/Luc, A20/Luc, and PG13 cells were previously described.[49–51] Cell line identity was confirmed by short tandem repeat (STR) profiling of highly polymorphic loci. All cell lines were routinely tested and confirmed to be mycoplasma-free.

Experimental animals

Female BALB/c mice (6–8 weeks old) and immunodeficient NXG mice (NOD-*Prkdc*^{scid}-*IL2rg*^{Tm1}/Rj, 6–8 weeks old) were obtained from janvier Labs. All mice were housed under specific pathogen-free (SPF) conditions in individually ventilated cages at the Animal Center of University Hospital Regensburg, with a 12-hour light/dark cycle and ad libitum access to food and water. All animal experiments were performed in accordance with institutional and national guidelines and were approved by the Animal Ethics Committee of University Hospital Regensburg and the Animal Ethics Committee of the Government of Lower Franconia (protocol numbers RUF-55.2.2-2532-2-1563 and RUF-55.2-2532-2-1838).

METHOD DETAILS

Sample collection

129 patients who received CAR-T cell therapy at the departments of Internal Medicine III of the University Hospital Regensburg (Regensburg, Germany), Internal Medicine III of the LMU University Hospital (Munich, Germany) and Internal Medicine V, Hematology, Oncology and Rheumatology of the University Hospital Heidelberg (Heidelberg, Germany) were enrolled in this analysis upon informed, written consent. Patient characteristics are summarized in Table 1. The data on disease- and treatment-courses were assessed during inpatient therapy and regular outpatient visits. Stool and serum samples were longitudinally collected at the time of hospital admission for CAR-T cell therapy and subsequent timepoints (e.g. day +7, day +14). Samples were stored at -80 °C until analysis (Figure 1A).

Mass spectrometry-based quantitation of metabolite levels

Serum and stool samples were prepared, processed, and quality-controlled as previously described.[73] Analysis was performed using a QTRAP 6500+ or QTRAP 5500 triple quadrupole mass spectrometer coupled to an ExionLC AD ultrahigh performance liquid chromatography system (both Sciex, Darmstadt, Germany). Data acquisition and instrument control were outlined using Analyst v1.7 (Sciex), and results were processed with MultiQuant v3.0.3 (Sciex) and MetaboAnalyst (Wishart Research Group, University of Alberta).

Human T cell isolation and activation

Peripheral blood mononuclear cells from healthy voluntary donors were obtained from the Department of Transfusion Medicine, University Hospital Regensburg after informed consent (ethic vote #21-2224-101 Regensburg). Cells were isolated by density gradient centrifugation (Pancoll™ Cell Separation Medium, PAN-Biotech, Germany) and negative magnetic separation (Pan T Cell Isolation Kit, human, Miltenyi Biotec, Germany). Purified T cells were then activated by adding T Cell TransAct™ (Miltenyi Biotec, Germany) at a 1:100 ratio to CAR-T cell medium. The medium consisted of RPMI 1640 (PAN Biotech, Germany) supplemented with 10% FBS, 2 mM GlutaMax, 100 U/mL penicillin-streptomycin, 10 mM HEPES, 1 mM sodium pyruvate and 1% MEM Non-Essential Amino Acid Solution (all Thermo Fisher Scientific, United States).

Murine T cell and blood isolation

Spleens were harvested from wild-type BALB/c mice (Janvier Labs, France) and mechanically dissociated. Splenocytes were collected by centrifugation, and red blood cells were lysed using RBC Lysis Buffer (iNtRON Biotechnology, South Korea) for 2 minutes at room temperature. Pan T cells were isolated using the Pan T Cell Isolation Kit II (Miltenyi Biotec, Germany) following the manufacturer's protocol. To evaluate the expansion of injected CAR-T cells in the murine CD19^{+} A20/Luc syngeneic model, whole blood was collected from the submandibular vein into EDTA-coated tubes and transferred into 96-well round-bottom plates (maximum 50 µL per well) for further processing. Red blood cells were lysed by adding 200 µL RBC Lysis Buffer for 5 minutes at room temperature, followed by centrifugation at 1,000g for 2 minutes. The supernatant was discarded, and the lysis step was repeated once. Residual lysis buffer was inactivated by adding staining buffer (PBS with 2% FBS), and cells were subsequently stained for flow cytometric analysis (for gating see Data S2).

Lentivirus production

HEK293T cells were used to produce pantropic, VSV-G pseudo-typed, second-generation lentivirus via multi-plasmid transfection. Cells at 80%–90% confluence were plated at a density of 3×10^5 cells/mL in 10 mL complete medium (DMEM-high glucose (Sigma-Aldrich, Germany) supplemented with 10% FBS and 100 U/mL penicillin-streptomycin) on 10 cm tissue culture plates (Corning, United States). The cells were evenly distributed by gentle swirling and incubated overnight. One hour before transfection, the medium was replaced with fresh, antibiotic-free DMEM-high glucose containing 10% FBS. Lentivirus was generated by lipid-mediated transient transfection using the Lipofectamine 3000 Kit (Thermo Fisher Scientific, United States). Each plate was transfected with 10 μg of packaging plasmid psPAX2 (Addgene plasmid #12260), 5 μg of envelope plasmid pMD2.G (Addgene plasmid #12259), and 10 μg of transfer plasmid carrying the gene of interest. The transfer plasmid, pHR_SFFv_4D5-Low-CAR_RHL001, encodes an anti-HER2 CAR, which was a gift from Wendell Lim (Addgene plasmid #164824).[74] Plasmids were isolated using the Pure Link HiPure Plasmid Midiprep Kit (Thermo Fisher Scientific Scientific, United States). Twenty-four hours after transfection, the medium was exchanged to complete medium, and the cells were incubated for another 24 hours before supernatant collection. The supernatant was centrifuged at 1,000g for 10 minutes at room temperature to remove cell debris, then filtered through a 0.45 μm membrane filter. Next, 38 mL of supernatant was transferred into Ultra-Clear centrifuge tubes (Beckman Coulter, United States). Ultracentrifugation was performed at 50,000g for 120 minutes at 4 °C using the SW 32 Ti swinging-bucket rotor in the Optima XE-90 ultracentrifuge (Beckman Coulter, United States), and the supernatant was discarded. Each pellet was resuspended in 200 μL of PBS. Aliquots of the concentrated virus were stored at -80 °C. Functional viral titers were determined using HEK293T cells.

Lentiviral human T cell transduction

Three days after activation, isolated T cells were transduced with lentivirus encoding the anti-HER2 CAR: 1.5×10^6 lentiviral particles in 500 μL CAR-T cell medium were centrifuged onto RetroNectin-coated (Takara Bio, Japan) 24-well plates at 32 °C and 1,500g for 2 hours. Next, the viral supernatant was removed. Next, 1×10^6 activated T cells were suspended in 1 mL CAR-T cell medium supplemented with IL-7 (10 ng/mL) and IL-15 (5 ng/mL, both Miltenyi, Germany) per well and centrifuged onto the plate at 320g for 5 minutes. The following day, transduced T cells were harvested and the transduction efficiency was evaluated using flow cytometry by staining the myc-tag in the extracellular CAR domain (Miltenyi anti-myc FITC, 130-116-653, 1:100).

Retroviral human T cell transduction

Retroviral transduction was carried out as described before.[50] Briefly, activated T cells were transduced using RetroNectin-coated plates on day 2 and day 3 after activation utilizing the retroviral supernatant derived from the PG13 producer cell line. The following day, the CAR single-chain variable fragment (scFv) was stained with an anti-FMC63 FITC antibody (AcroBiosystems, FM3-FY45P1, 1:100) to evaluate the transduction efficacy.

Murine CAR-T cell production

Purified T cells were plated in 96-well round-bottom plates (4×10^4 cells/well; Corning, United States) and stimulated with anti-CD3/CD28 beads (2 beads/cell, Miltenyi Biotec, Germany) in the presence of 100 U/mL IL-2 (PeproTech, United States) in mouse T cell medium. The medium consisted of DMEM-high glucose (Sigma-Aldrich, Germany) supplemented with 10% FBS, 100 U/mL penicillin-streptomycin, 0.05 mM 2-mercaptoethanol, 10 mM HEPES, and 1% each of MEM Vitamin and Non-Essential Amino Acid Solutions (all Thermo Fisher Scientific Scientific, United States). Retroviral transduction was performed after 24 hours of activation.

To produce retroviral particles, Phoenix-Eco cells were seeded onto gelatin-coated 6-well plates at 5×10^5 cells/mL (2 mL/well) and transfected 6 hours later using TransIT-293 (Mirus Bio, United States). For each well, 1 μg of pCL-Eco packaging plasmid and 3 μg of pMSCV_1D3_CD28z_CD90.1 (encoding a murine anti-CD19 CAR (sequence RRID: Addgene_107227[75] and CD90.1 marker) were mixed with 12 μL TransIT-293 in OptiMEM (both Thermo Fisher Scientific, United States) and incubated for 20 minutes at room temperature before transfection. Medium was replaced after 16 hours, and viral supernatants were collected 24 hours later, centrifuged (4,000g, 10 minutes, room temperature), and supplemented with 24 μg/mL Polybrene (Sigma, Germany).

For transduction, 100 μL of viral supernatant was added to pre-activated murine pan T cells (40,000/well) in 96-well round-bottom plates. After 6.5 hours, 160 μL of medium was replaced with fresh T cell medium containing 100 U/mL IL-2. Three days later, T cells were harvested, beads removed via magnetic separation (Miltenyi Biotec, Germany), and cells rested for 24 hours in mouse T cell medium containing 100 U/mL IL-2. Transduction efficacy was assessed by staining with an anti-CD90.1 BV421 antibody (BioLegend, United States, 202529, 1:100) and cells were washed, counted, and prepared for adoptive transfer.

Cas9 ribonucleoprotein-based gene editing

Gene editing in (CAR-) T cells was carried out by nucleofection of Cas9 protein with aligned tracr and crRNA (IDT) using the Lonza 4D nucleofection system with the P3 Primary Cell 4D-Nucleofector™ X Kit using the CA137 program following the manufacturers guidelines. Guide RNAs were designed with Benchling (Benchling, United States) and were 5′-TCAAGTCAAATCCTTCCAAG-3′ and 5′-CATCTTGTGGGAAAGGCAGC-3′ for the *AHR* gene.

IMM handling, dilution, carrier control and dosing

All metabolites were pH-neutralized utilizing NaOH to pH 7 to avoid confounding effects of acidity. Indole-3-carboxaldehyde (ICA) and indole-3-acetic acid (IAA) were prepared as 500 mM stock solutions in DMSO and diluted into culture medium, resulting in a maximal final DMSO concentration of 0.1%. Valeric acid and isovaleric acid were prepared as 200 mM aqueous stock solutions, yielding a maximal final H_2O concentration of 0.5% after dilution in medium. To ensure full comparability across conditions, all treatments – including controls – were adjusted to contain 0.1% DMSO and 0.5% H_2O. For the *in vivo* experiments, metabolites were dissolved in either DMSO (ICA) or water (valeric acid and isovaleric acid). The respective volumes of each metabolite stock were combined and adjusted with vehicle components to obtain a final mixture containing 20% DMSO, 40% PEG400 (Sigma, Germany), and 40% sterile water. A total volume of 200 μl of this formulation, containing the final concentrations indicated below, was administered to each mouse via gavage. We selected metabolite concentrations based on previous publications that also reflect typical fecal levels in antibiotic naïve patients in our cohort (with 1 μmol/g feces approximately corresponding to 1000 μM concentration; Figures S2A–S2C) for *in vitro* assays.[11,13,14,76,77] For *in vivo* analyses, we utilized metabolite quantities that were previously published to exert biologically relevant effects.[13,76–78]

Cell lysis assays

CAR-T cell killing efficiency was evaluated using a bioluminescence assay. CAR-T cells were pretreated in CAR-T cell medium supplemented with IL-7 (10 ng/mL) and IL-15 (5 ng/mL, both Miltenyi, Germany) and the indicated metabolites (or their carrier as control) for 72 hours. SKOV3 or NALM-6 target cells were seeded in white 96-well plates at 25,000 cells/well, followed by the addition of metabolite-treated CAR-T cells at an effector-to-target (E:T) ratio of 1:5 in 200 μL of CAR-T cell medium without interleukins. After 48 hours 50 μL IVISbrite™ D-Luciferin (150 μg/mL, Revvity, Germany) was added and cells were incubated at 37 °C for 10 minutes before luminescence was measured on a Tecan Spark plate reader (Tecan Group, Germany). Cell lysis was calculated as: % lysis = [1 − (mean luminescence in treated wells / mean luminescence in control wells)] × 100%.

Protein-based CAR-T cell stimulation and flow cytometry

To directly stimulate anti-HER2 or anti-CD19 CAR-T cells via their cognate antigen, 96-well round-bottom plates were coated with recombinant human HER2/ERBB2 protein (ECD, hFc-tag; Sino Biological, China) at 0.1 μg/mL or recombinant human CD19 protein (ECD, His & AVI Tag; Sino Biological, China) at 0.5 μg/mL in 200 μL PBS and incubated for 18 hours at 4 °C. Plates were then washed with PBS to remove unbound protein. Anti-HER2 CAR-T cells or anti-CD19 CAR-T cells (1×10^5 cells/well) were added in the presence of metabolites or carrier and cultured for 72 hours at 37 °C, 5% CO_2 in CAR-T cell medium containing 100 U/mL IL-2 (Milteniy, Germany).

For intracellular cytokine staining, cells were treated with Cell Stimulation Cocktail plus protein transport inhibitor (Thermo Fisher Scientific, United States) for 4 hours. Dead cells were stained with Zombie UV Fixable Viability Kit (BioLegend, United States, 423108, 1:200) or Fixable Viability Dye eFluor 780 (Thermo Fisher Scientific, United States, 65-0865-18, 1:1,000) for 20 minutes at 4 °C. Fc receptor blocking was performed using Blocking Buffer (PBS + 10% FBS) for human samples or anti-mouse CD16/CD32 antibody (BioLegend, United States, 101302, 1:100) for murine samples for 15 minutes at 4 °C. Surface staining was conducted in Staining Buffer supplemented with 20% Brilliant Stain Buffer (BD Biosciences, United States), using a 25 μL antibody cocktail per well for 30 minutes at 4 °C. Intracellular staining was carried out using the Foxp3/Transcription Factor Staining Buffer Set (Thermo Fisher Scientific, United States). Cells were fixed for 40 minutes at room temperature and washed twice with Permeabilization Buffer before and after staining with intracellular antibodies, which were diluted in Permeabilization Buffer containing 20% Brilliant Stain Buffer. Final staining was performed in 25 μL for 40 minutes at room temperature. Details on antibodies used for staining are listed in the key resources table. Samples were acquired on a FACSymphony A5 or FACSCelesta Cell Analyzer (BD Biosciences, United States). For gating strategies see Data S2.

Single-cell RNA sequencing (scRNA-seq) with 10x Genomics GEM-X

To assess the effects of metabolite treatment on gene expression in anti-HER2 CAR-T cells, scRNA-seq was performed. Anti-HER2 CAR-T cells from four donors were stimulated on HER2 protein-coated plates for 3 days in the presence of ICA (500 μM), isovaleric acid (1,000 μM), valeric acid (1,000 μM), or carrier control (16 samples total). For each sample 9,000 anti-HER2 CAR-T cells were sorted on a FACSAria™ Fusion (BD Biosciences, United States, for gating see Data S2) and loaded into individual lanes of the Chromium GEM-X OCM 3′ChIP v4plex chip and processed using the GEM-X Universal 3′ Gene Expression v4 4-plex Kit (both 10x Genomics, United States) per manufacturer's instructions. Amplified cDNA was used to prepare 3′ scRNA-seq libraries, which were quantified by Qubit (Thermo Fisher Scientific, United States) and quality assessed by TapeStation (Agilent, United States) measurement. Libraries were sequenced on a NextSeq 2000 Sequencer (Illumina, United States) with PE-28-10-10-90 read configuration.

scRNA-seq raw read processing

Base-calling and demultiplexing of sequencing reads was carried out using *bcl2convert* v3.8.4 (*Illumina Dragen*, NextSeq2000, Illumina Inc., United States). Sequencing reads were processed using the multi command from *Cell Ranger* v9.0.1 (10x Genomics,

United States) with default parameters to align to the human genome (GRCh38), call cells, and generate UMI count matrices for gene expression libraries. The multi-configuration CSV file mapped treatment conditions to on-chip-multiplexing barcoding groups for each library.

scRNA-seq data analysis

Single-cell RNA-seq data analysis was performed in R v4.3.0 using *Seurat* v5.0.1.[79] Preprocessing, filtering, and clustering were executed via *RMarkdown* v2.25 scripts orchestrated by a *Snakemake* v5.18.0 pipeline (Python v3.9.7).

Doublets were detected per sample (donor–treatment) with *scDblFinder* v1.14.0[66] (with *SingleCellExperiment* v1.22.0) in random mode and removed. Cells with total RNA counts >1,000, features >200, and mitochondrial gene percentage <10% were retained (46,653 of 53,272 *Cell Ranger* calls). UMI counts were library-size normalized and ln(1+x)–transformed. The 2,000 most variable genes were selected with *Seurat*'s FindVariableFeatures() (vst method). Data were mean-centered, scaled to unit variance, and S-phase/G2M effects regressed out using *UCell*[80] scores (signatures from *Tirosh et al.*,[81]). PCA was performed, and *Harmony* v1.2.0[54] integration (default parameters, grouped by library/donor) was performed to correct for batch effects.

For clustering, *Seurat*'s FindNeighbours() and FindClusters() were applied to the first 20 *Harmony*-corrected PCs (Louvain, default parameters), and *UMAP*[82] was computed using *Seurat*'s RunUMAP() function on the same PCs; clustering resolution 0.35 was chosen for downstream analyses.

Cell types were annotated using *Azimuth* v0.5.0 with the *pbmcref* PBMC reference dataset,[67] combined with manual marker-based inspection. Analysis for differential cell type abundance (DA) between treatment groups was performed with the *MASS* R-package (v7.3.60).[83] Briefly, for each cell type from the annotated scRNA-seq data, a negative binomial model with the variables treatment group and library/donor was fitted to the cell count data. Total cell count per sample (i.e., library size) was used as an offset for normalization. P-values were derived by performing a Wald test with the respective linear contrasts of model parameter estimates. They were then adjusted for multiple testing using the FDR approach across all hypotheses within a given cell type.

Differential gene expression between treatment groups within CD4 or CD8 subsets was assessed on raw counts using *NEBULA* v1.5.3[63] (negative binomial gamma mixed model) with treatment group and library/donor as variables. Each combination of treatment group and donor was considered a distinct subject. Library size was set as the scaling factor (normalization), and minimum counts per cell for a gene to be tested were set to 0.005 (*NEBULA-LN* method; defaults otherwise). Gene set enrichment analysis[61] using *fgsea* v1.26.0 was performed on signed –log10 p-values signed by log fold-change from *NEBULA* results; gene sets were obtained via *msigdbr* v7.5.1 from the Hallmark (H), KEGG, Wikipathways, Reactome (C2) and GO Biological Process (C5) collections of *MSigDB*.[62] Only sets with $\geq$70% gene coverage were tested; p-values were FDR-adjusted to 10% per gene set collection and comparison. Code used to perform the scRNA-Seq analysis has been deposited on GitHub and can be accessed at https://github.com/lit-regensburg/scRNA_CAR_T_metabolites and results tables can be found in Data S3.

Bulk RNA sequencing (bulk RNA-seq)

A20/Luc lymphoma cells were seeded at 1x10^5 cells/mL in 4 mL RPMI 1640 supplemented with 2 mM L-glutamine, 10% FBS, 100 U/mL penicillin-streptomycin, and 0.05 mM 2-mercaptoethanol in 6-well plates. Cells were incubated for 3 days at 37 °C and 5% CO_2 in the presence of 1000 μM valeric acid, isovaleric acid, or carrier control. For RNA isolation, cells were collected into 15 mL Falcon tubes and pelleted at 300 g for 10 min. The pellets were washed with cold PBS, centrifuged again at 300 g for 10 min, and the supernatant was removed. Samples were resuspended in 350 μL Buffer RLT containing 2% DTT. Total RNA was isolated using the RNeasy Mini Kit (Qiagen) and RNA quality was assessed on a 4200 TapeStation using High-Sensitivity RNA ScreenTape (Agilent). Libraries were prepared from 500 ng total RNA using the QuantSeq 3′ mRNA-Seq Library Prep Kit (Lexogen) according to the manufacturer's instructions. Briefly, first-strand synthesis was initiated by oligo(dT) priming, followed by second-strand synthesis using random priming; libraries were purified with magnetic beads, PCR-amplified, and indexed with unique dual indices. Libraries were quantified by TapeStation D1000 and Qubit, pooled equimolarly, and sequenced as single-end reads on an Illumina NextSeq 2000 (P2, 100 cycles).

CAR-T cell proliferation assay

To assess CAR-T cell proliferation, anti-HER2 CAR-T cells were labeled with 2 μM CellTrace™ CFSE (Thermo Fisher Scientific, United States) following the manufacturer's instructions. Labeled cells were plated at 1×10^5 cells per well in recombinant human HER2/ERBB2 protein-coated 96-well plates and incubated at 37 °C with 5% CO_2 for 3 days in the presence of metabolites at the indicated concentration in CAR-T cell medium containing 100 U/mL IL-2. Following stimulation, cells were washed to remove residual HER2/ERBB2 protein and cultured for 4 days in fresh medium. CFSE dilution was assessed by flow cytometry on day 7 to quantify cell division (for gating see Figure S5A).

SCENITH assay of artificially stimulated anti-HER2 CAR-T cells

The SCENITH (Single Cell ENergetIc metabolism by profiling Translation Inhibition) assay,[21] was used to functionally assess metabolic reprogramming in anti-HER2 CAR-T cells. Cells were artificially stimulated on HER2 protein coated plates for 72 hours in presence of IAA, ICA, valeric and isovaleric acid, or carrier control at the indicated concentrations. After stimulation, cells were plated at 1×10^6 cells/mL in antibiotic-free RPMI (100 μL/well) in flat-bottom 96-well plates. Experimental duplicates were included for all

conditions. Following a 1-hour rest at 37 °C and 5% CO_2, cells were treated for 15 minutes with 2-deoxy-D-glucose (2-DG; 100 mM; Sigma-Aldrich), harringtonine (2 μg/mL; Santa Cruz Biotechnology), or DMSO control. Puromycin (10 μg/mL; Sigma-Aldrich) was then added for 25 minutes. Subsequently, cells were washed with cold PBS and stained intracellularly for flow cytometry to detect puromycin incorporation in anti-HER2 CAR-T cells (for gating see Data S2).

Total protein translation was calculated as puromycin MFI (DMSO − harringtonine). Glucose dependence was calculated as puromycin MFI ((DMSO − 2-DG)/(DMSO − harringtonine)) × 100. Fatty acid oxidation (FAO) and amino acid oxidation (AAO) capacity were defined as 100 − glucose dependence (%). All values were normalized to matched donor carrier-treated controls.

Immuno-Western Blot

Human anti-HER2 CAR-T cells were treated for 24 h with 1000 μM valeric/isovaleric acid or carrier, lysed in RIPA buffer, and 10 μg total protein separated on 12% TGX gels (Bio-Rad, United States). Proteins were transferred to PVDF using the Trans-Blot Turbo system (Bio-Rad), blocked, and probed overnight (4 °C) with primary antibodies (Cell Signaling Technology, United States) against p-mTOR (S2448), p-S6 (S235/236), p-ACC (Ser79), p-PDHA1 (Ser293), H3K9ac (all 1:1,000), or β-actin (1:10,000). After secondary HRP incubation (2 h, RT) and development with Femto ECL (Thermo Fisher Scientific, United States), images were acquired via Image Lab (Bio-Rad). Membranes were stripped with ReBlot Plus (1X; Merck Millipore, United States) and reprobed for mTOR, S6, ACC, PDHA1, and H3 (Cell Signaling Technology, 1:1,000). Phosphorylation was quantified as the ratio of phospho- to total protein band intensity using Image Lab software (Bio-Rad). Raw scans are available in Data S4.

HDAC2 Inhibition Assay

To determine the HDAC2-inhibitory capacity of valeric acid (VA) and isovaleric acid (IVA), HDAC2 activity was measured using the fluorogenic HDAC2 Assay Kit (BPS Bioscience, United States) according to the manufacturer's instructions. Valeric acid and isovaleric acid were tested at 0.1, 0.5, 1, 2.5, and 5 mM, and Trichostatin A (20 μM) was used as a control inhibitor.

Bioluminescence-based proliferation assay

A20/Luc lymphoma cells were seeded at 1×10^5 cells/mL in 1 mL RPMI 1640 supplemented with 2 mM L-glutamine, 10% FBS, 100 U/mL penicillin-streptomycin, and 0.05 mM 2-mercaptoethanol. Cells were cultured with valeric or isovaleric acid or carrier at the indicated concentrations in non-tissue culture–treated 24-well plates. On days 0, 3, and 5, 200 μL of cell suspension was transferred to a white 96-well plate and incubated with 50 μL of IVISbrite™ D-Luciferin (final concentration 150 μg/mL) for 10 minutes at 37°C. Luminescence was measured using a Spark plate reader (Tecan).

Animal experiments

In the murine $CD19^+$ A20/Luc syngeneic model female BALB/c mice (10–12 weeks old; Janvier Labs, France) were randomly assigned to treatment groups and received daily oral gavage of metabolites (400 mg/kg of valeric acid or isovaleric acid and 150 mg/kg of ICA in a final volume of 200 μL) or carrier beginning four days (day-4) prior to CAR-T cell injection and continuing for 19 days. On day −3, mice were conditioned with 4.5 Gy total body irradiation, followed by intravenous injection of 1×10^6 A20/Luc lymphoma cells via the tail vein. To evaluate the effects of metabolite treatment, mice received 2.5×10^5 anti-CD19 CAR-T cells intravenously on day 0; untransduced Pan T cells served as controls. Tumor progression and treatment response were monitored via bioluminescence imaging (BLI) using a Xenogen IVIS system (PerkinElmer, United States) following intraperitoneal injection of 100 μL IVISbrite™ D-Luciferin (30 mg/mL, Revvity, Unites States). Tumor burden was quantified as total flux (photons/second). Peripheral blood was collected every two weeks via submandibular vein puncture to assess CAR-T cell expansion by flow cytometry.

To determine direct effects of metabolite treatment on A20/Luc lymphoma cell growth and disease progression, the same model as described above was used but no CAR-T cells were injected. Mice that did not engraft tumor before day 60 after A20/Luc cell injection (determined by bioluminescent imaging) were taken out of the analysis.

For the additional murine $CD19^+$ A20/Luc experiment, female BALB/c mice were used as described above, except that CAR-T cells were pretreated *in vitro* with 1000 μM valeric acid, isovaleric acid, or carrier for 72 h before injection, and tumor cell injection preceded CAR-T cell transfer by 5 days.

In the human $CD19^+$ NALM-6 xenograft model, female NOD-*Prkdc*^{scid}-*IL2rg*^{Tm1}/Rj (10–12 weeks old; Janvier Labs, France) were randomly assigned to treatment groups and received daily oral gavage of 150 mg/kg ICA, 400 mg/kg isovaleric acid or carrier control (in 200 μL) starting 4 days prior to CAR-T cell injection (day -4) and continuing for 19 days. On day -3, mice were injected intravenously with 0.5×10^6 NALM-6/GFP-Luc cells. On day 0, mice received 1×10^6 AHR-deficient (CRISPR-Cas9 knockout) or Cas9-control human anti-CD19 CAR-T cells (in the ICA Experiment) or WT human anti-CD19 CAR-T cells (in the isovaleric acid experiment) via intravenous injection; tumor-bearing mice that did not receive CAR-T cells served as controls. Tumor progression and treatment response were monitored as described above for the A20 model.

Mice were monitored daily, and humane endpoints were defined as surrogate survival criteria or 80 days (A20 model) or 60 days (NXG model) post-treatment. Animals were euthanized upon reaching these endpoints. Of note, mice meeting euthanasia criteria despite undetectable IVIS signal were subjected to necropsy to confirm tumor presence.

Metabolite Bioavailability Assay

Metabolites were administered via single oral gavage as a cocktail containing 400 mg/kg of valeric acid, isovaleric acid and 150 mg/kg of ICA in a final volume of 200 μL. Stool, heart blood, and portal vein blood were collected 30 min post-gavage. Metabolite concentrations were determined by mass spectrometry.

Metagenomic Sequencing

DNA was isolated from stool samples after bead beating with Lysing Matrix B prefilled bead tubes (MP Biomedicals, Germany) using the Maxwell® RSC Fecal Microbiome DNA Kit in a Maxwell device (Promega, United States). Samples of 1 μg of genomic DNA are randomly fragmented (∼ 350 bp) using a Covaris ultrasonic disruptor (Covaris, United States). Fragments are end repaired and A-tailed. Sequencing adapters (i.e., P5 and P7 according to Illumina, United States) are ligated and the fragments are purified from remaining adapters. DNA is amplified with PCR and the size of the fragments between adapters are assessed using an AATI analyzer (Agilent, United States). The effective library is quantified using qPCR and libraries are pooled according to their effective concentrations and target data output requirements and then subjected to PE150 sequencing. Sequencing is conducted using a NovaSeq Xplus series 25B (Illumina, United States) with PE150. Adapters are removed from raw reads during dereplication of the reads for each sample.

Plotting and Statistics

Data analysis was performed with R (v4.4.2) using tidyverse[71] (v2.0.0). In addition, ggprism (v1.0.6), ggpubr (v0.6.0), patchwork (v1.3.0), ggrepel (v0.9.8) and ggbeeswarm (v0.7.2) were used to generate plots. RColorBrewer (v1.1-3) and colorspace (v2.1-1) were used for color palette generation. Statistical analysis was conducted using the rstatix (v0.7.2) package. The script used to perform and plot the metagenomics and metabolomics analysis has been deposited on GitHub available under https://github.com/lit-regensburg/IMM-CART-Paper_MGX-MBX.

Survival Curves

Progression free survival (PFS) was defined as the time between CAR-T cell treatment and progression of the underlying disease or death from any cause and is presented as a Kaplan-Meier curve with differences between groups calculated using the log-rank test and the hazard ratio calculated with a Cox proportional hazards regression model utilizing the survival (v3.8-3) and survminer (v0.5.0) packages. If not stated otherwise, cutpoint thresholds were calculated using the maximum rank statistic against PFS with the surv_cutpoint function from the survminer package.

Metagenomic Data Analysis

The metagenomic raw reads were processed by removing the adapters and trimming sequences using Trim Galore[72] with the following parameters: –phred33 -quality 30 -stringency 5 -length 10. Afterwards, Kneaddata (https://github.com/biobakery/kneaddata) was used for quality filtering and host sequences decontamination, with the parameters: "-trimmomatic-options HEADCROP:15 SLIDINGWINDOW:4:15 MINLEN:50" and default parameters. The taxonomic abundance profiling was estimated by MetaPhlAn 4.1.1 with default parameters.[59] The functional profiles of microbial community were identified using HUMAnN3 with default parameters.[55]

Alpha diversity metrics (Richness: observed richness, Diversity: Shannon diversity and Dominance: Berger-Parker Index for dominance) were calculated using phyloseq[64] (v1.50.0) and microbiome (v1.28.0) R packages. The means were compared using a two-sided Wilcoxon rank sum test. Thresholds for grouping richness, diversity and dominance into "high" and "low" bins were defined as the lower respective quartile.

Associations between microbial taxa (species and genera) and clinical outcomes (CR d180, PFS, OS) were investigated in R using multiple approaches: Linear Discriminant Analysis Effect Size (LEfSe[57]) was performed using the lefser package (v1.16.2). For the univariate Cox proportional hazards models and LASSO-penalized Cox models only species and genera with a prevalence of at least 20% across samples were included. The Cox PH models were fitted using the survival package (v3.8-3) and LASSO-penalized Cox models were generated with glmnet (v4.1-8[53]) applying 10-fold cross validation. Differential abundance testing with LinDA was performed utilizing MicrobiomeStat (v1.4.1).[60] Finally, MaAsLin3 (v0.99.16[58]) was used with default settings, including the clinical outcome as the sole predictor. Previously described species and genera associated to outcomes of CAR-T cell treatments were derived from Marcos-Kovandzic et al.[18], Stein-Thoeringer et al.[8], Smith et al.[9] and Hu et al.[10]The effect of these bacteria in our cohort was tested with a univariate Cox proportional hazard model. The effect direction was compared with the published direction using a method based on ROC curves, utilizing the pROC (v 1.18.5) package.

Bray-Curtis dissimilarity is calculated using the distance function from the phyloseq package. It was visualized using the pheatmap (v1.0.12) package. The NMDS and PCoA ordination was calculated and plotted also using functions from the phyloseq package. Group differences were tested with PERMANOVA using the adonis2 function from the vegan (v2.6-10) package.

Hazard ratios of bacterial pathways were calculated using univariate Cox proportional hazard models. The top ten most significant positive and negative hazard ratios were plotted.

Metabolite Data Analysis

Metabolites not measured across all batches due to panel adjustments, as well as metabolites with >90% of samples below the detection threshold, were excluded from analysis. Below detection threshold-values of the other metabolites were imputed by half minimum of the respective metabolite before being log2 transformed and batch corrected with the ComBat function from the sva package (v3.54.0), explicitly retaining information about the disease category and antibiotics pretreatment in the model. After batch correction the data was transformed back to non-log values. The means between metabolite concentrations in antibiotics and non-antibiotics treated patients were compared using a two-sided Wilcoxon rank sum test. Outliers were defined as datapoints with at least two standard deviations distance to the mean and were omitted during plotting, while they were included in statistical tests.

Metabolite concentrations for the heatmap and principal component analysis were winsorized (5%/95% quantile cutoff) using the Winsorize function from the DescTools (v0.99.60) package and z-scaled. Hierarchical clustering was performed using euclidean distances and the ward.D2 clustering method. The heatmap was plotted using the pheatmap package.

Bulk RNA-seq Data Analysis

RNA sequencing reads were processed using snakepipes[68] (v2.5.1) mRNA-seq workflow with the following parameters: "—trim—fastqc—trimmer trimgalore—trimmerOptions—clip_R1 12 -m alignment—libraryType 1—bcExtract—bcPattern NNNNNN—UMIDedup—UMIDedupOpts output-stats". In short this resulted in adapter and quality trimming with TrimGalore (v0.6.5), with an additional 12 bp clipped from the 5′ end as recommended for the Lexogen QuantSeq 3′ mRNA-seq Library Prep Kit. Reads were mapped to the GRCm38 genome (Gencode release 23) using STAR[69] (v2.7.4). PCR duplicate removal was performed using UMI-tools (v1.0.1) based on unique molecular identifiers (UMIs). Read counts per gene were extracted using featureCounts/Subread[70] (v2.0.0).

Exploratory and differential gene expression analysis was performed using DESeq2 (1.50.2) with assistance from DEGreport (v1.46.0). Genes were filtered to retain those with a count of at least one in each sample. For exploratory analysis, gene expression was normalized using regularized log transformation, and principal component analysis (PCA) was performed using the 100 most variable genes. Genes were annotated using AnnotationDbi (v1.72.0) with org.Mm.eg.db (v3.22.0). Gene set enrichment analysis was performed using clusterProfiler[52] (v4.18.4) with Gene Ontology Biological Process terms from org.Mm.eg.db. Redundancy among enriched terms (p.adjust < 0.05) was reduced using rrvgo[65] (v1.22.0). A similarity space map of enrichment results with minimum edge similarity threshold of 0.15 was generated using enrichplot (v1.30.5), and cluster labels were assigned manually based on representative terms. Complete results tables for differential gene expression and gene set enrichment analyses are provided in Data S5. Code for analysis and visualization has been deposited in the GitHub repository: https://github.com/lit-regensburg/IMM-CART-Paper_RNASeq-A20.

Risk Score

The risk score was derived from stool concentrations of valeric acid, isovaleric acid, IAA, and ICA, or from serum concentrations of valeric acid, isovaleric acid and IAA. Metabolite-specific thresholds were determined using the maximum rank statistic in relation to PFS. A score of 1 was assigned if the beneficial metabolite (valeric acid) was below its threshold or if any of the detrimental metabolites (isovaleric acid, IAA, and ICA) exceeded theirs, resulting in total scores ranging from 0 to 4 (stool) or 0 to 3 (serum). For Kaplan–Meier analysis, patients were stratified into low-risk (scores 0–3 for stool, 0–2 for serum) and high-risk (score 4 for stool, 3 for serum) groups. Differences between groups were assessed using a univariate Cox proportional hazards model. The performance of the risk score was evaluated against PFS events using receiver operating characteristic (ROC) and precision-recall (PR) curves, implemented via the pROC (v1.18.5) and precrec (v0.14.5) packages. To assess the independent prognostic value of the risk score, a multivariate Cox proportional hazards regression model was fitted, incorporating the ordinal risk score along with clinically relevant covariates: center (Regensburg, Heidelberg, München), CAR-T costimulatory domain (41BB, CD28), disease type (non-Hodgkin lymphoma (NHL), multiple myeloma (MM) and other including solid tumors), antibiotics exposure (antibiotics, no antibiotics), cytokine release syndrome (CRS) grade (0–4), sample timing (days to treatment), sex (male vs. female), age (years), lactate dehydrogenase (LDH), and Eastern Cooperative Oncology Group (ECOG) performance status (0–4). Age and LDH values were z-transformed prior to modeling.

QUANTIFICATION AND STATISTICAL ANALYSIS

Statistical analyses were performed using GraphPad Prism (version 10.6.1; GraphPad Software, San Diego, CA, USA) and R (version 4.5.1; R Foundation for Statistical Computing).

All statistical details, including definitions of n, statistical tests used, measures of central tendency and dispersion, and significance thresholds, are provided in the corresponding figure legends.